REPORT DOCUMENTATION PAGE

Form Approved OMB NO. 0704-0188

1. REPORT DATE (DD-MM-YYYY)	2. REPORT TYPE	3. DATES COVERED (From - To)
	New Reprint	-

4. TITLE AND SUBTITLE

Monolithic Hierarchical Fractal Assemblies of Silica Nanoparticles Cross-Linked with Polynorbornene via ROMP: A Structure–Property Correlation from Molecular to Bulk through Nano

5a. CONTRACT NUMBER
W911NF-10-1-0476

5b. GRANT NUMBER

5c. PROGRAM ELEMENT NUMBER
611104

6. AUTHORS

Dhairyashil P. Mohite, Zachary J. Larimore, H. Lu, Joseph T. Mang, Chariklia Sotiriou-Leventis, Nicholas Leventis

5d. PROJECT NUMBER

5e. TASK NUMBER

5f. WORK UNIT NUMBER

7. PERFORMING ORGANIZATION NAMES AND ADDRESSES

Missouri University of Science and Technology
Curators of the Univ. of Missouri on behalf of Missouri S&T
300 W. 12th Street
Rolla, MO 65409 -

8. PERFORMING ORGANIZATION REPORT NUMBER

9. SPONSORING/MONITORING AGENCY NAME(S) AND ADDRESS(ES)

U.S. Army Research Office
P.O. Box 12211
Research Triangle Park, NC 27709-2211

10. SPONSOR/MONITOR'S ACRONYM(S)
ARO

11. SPONSOR/MONITOR'S REPORT NUMBER(S)
58312-CH.23

12. DISTRIBUTION AVAILIBILITY STATEMENT

Approved for public release; distribution is unlimited.

13. SUPPLEMENTARY NOTES

The views, opinions and/or findings contained in this report are those of the author(s) and should not contrued as an official Department of the Army position, policy or decision, unless so designated by other documentation.

14. ABSTRACT

Monolithic hierarchical fractal assemblies of silica nanoparticles are referred to as aerogels, and despite an impressive collection of attrcative macroscopic proporties, gragility has been the primary drawback to applications. In that regard, polymer-cross-linked silica aerogels have emerged as strong lightweight nanostructured alternatives rendering new applications unrelated to aerogels before, as in balistic protection, possible. However, the exact location of the polymer ion the elementary structure of silica and, therefore, critical issues, such as how much is

15. SUBJECT TERMS

silica, serogel, cross-linking, mechanism, ROMP, norbornene, polymer, hierarchical, primary particles, secondary particles, SANS, SAXS, rheology

16. SECURITY CLASSIFICATION OF:			17. LIMITATION OF ABSTRACT	15. NUMBER OF PAGES	19a. NAME OF RESPONSIBLE PERSON
a. REPORT	b. ABSTRACT	c. THIS PAGE			Nicholas Leventis
UU	UU	UU	UU		19b. TELEPHONE NUMBER: 573-341-4391

Report Title

Monolithic Hierarchical Fractal Assemblies of Silica Nanoparticles Cross-Linked with Polynorbornene via ROMP: A Structure–Property Correlation from Molecular to Bulk through Nano

ABSTRACT

Monolithic hierarchical fractal assemblies of silica nanoparticles are referred to as aerogels, and despite an impressive collection of attrcative macroscopic proporties, gragility has been the primary drawback to applications. In that regard, polymer-cross-linked silica aerogels have emerged as strong lightweight nanostructured alternatives rendering new applications unrelated to aerogels before, as in balistic protection, possible. However, the exact location of the polymer ion the elementary structure of silica and, therefore, critical issues, such as how much is enough, have remained ambiguous. To address those issues, the internal nanoporous surfaces of silica wet-gels were modified with norbornene (NB) by cogelation of tetramethyl orthosilicate (TMOS) with a newly synthesized derivative of nadic acid (Si-NAD: N-(3-triethoxysilylpropyl)-5-norbornene-2,3-dicarbosimide). As inferred by both rheological and liquid 29-Si NMR data, Si-NAD reacts more slowly than TMOS, yielding a TMOS-derived skeletal silica network, surface-derivatized with NB via monomer-cluster aggregation. Then, ring-opening metathesis polymerization (ROMP) of free NB in the nanopores engages surface-bound NB moities and bridges skeletal nanoparticles either through cross-metathesis or a newly described stiching mechanism. After solvent exchange and drying with supercritical fluid CO2 into aerogels (bulk densities in the range 0.27-0.63 g cm-3, versus 0.20 g cm-3 of the native network), the bridging nature of the polymer is inferred by a >10-fold increase in mechanical strength and 4-fold increase in the energy absorption capability reative to the native samples. The crosslinking polymer was freed from silica by treatment with HF, and it was found by GPC that it consists of a long and short component, with around 400 and 10 monomer units, respectively. No evidense (by SAXS) was found for the polymer coiling up into particles, consistent with the microscpic similarity (by SEM) of both native and cross-linked samples. Most importantly, the polymer does not need to spill over higher aggregates for greatly improved mechanical strength; mechanical propoerties begin improving after the polymer coats primary particles. Extremely robust materials are obtained when the polymer fills most of the fractal space within secondary particles.

REPORT DOCUMENTATION PAGE (SF298)
(Continuation Sheet)

Continuation for Block 13

ARO Report Number 58312.23-CH
Monolithic Hierarchical Fractal Assemblies of Sil ...

Block 13: Supplementary Note

Approved for public release; distribution is unlimited.

CHEMISTRY OF MATERIALS

Article

pubs.acs.org/cm

Monolithic Hierarchical Fractal Assemblies of Silica Nanoparticles Cross-Linked with Polynorbornene via ROMP: A Structure−Property Correlation from Molecular to Bulk through Nano

Dhairyashil P. Mohite,[†] Zachary J. Larimore,[†] H. Lu,*[,‡] Joseph T. Mang,*[,§] Chariklia Sotiriou-Leventis,*[,†] and Nicholas Leventis*[,†]

[†]Department of Chemistry, Missouri University of Science and Technology, Rolla, Missouri 65409, United States

[‡]Department of Mechanical Engineering, The University of Texas at Dallas, Richardson, Texas 75080, United States

[§]Los Alamos National Laboratory, Los Alamos, New Mexico 87545, United States

Supporting Information

ABSTRACT: Monolithic hierarchical fractal assemblies of silica nanoparticles are referred to as aerogels, and despite an impressive collection of attractive macroscopic properties, fragility has been the primary drawback to applications. In that regard, polymer-cross-linked silica aerogels have emerged as strong lightweight nanostructured alternatives rendering new applications unrelated to aerogels before, as in ballistic protection, possible. In polymer-cross-linked aerogels skeletal nanoparticles are connected covalently with a polymer. However, the exact location of the polymer on the elementary structure of silica and, therefore, critical issues, such as how much is enough, have remained ambiguous. To address those issues, the internal nanoporous surfaces of silica wet-gels were modified with norbornene (NB) by cogelation of tetramethyl orthosilicate (TMOS) with a newly synthesized derivative of nadic acid (**Si-NAD**: *N*-(3-triethoxysilylpropyl)-5-norbornene-2,3-dicarboximide). As inferred by both rheological and liquid ^{29}Si NMR data, **Si-NAD** reacts more slowly than TMOS, yielding a TMOS-derived skeletal silica network surface-derivatized with NB via monomer-cluster aggregation. Then, ring-opening metathesis polymerization (ROMP) of free NB in the nanopores engages surface-bound NB moieties and bridges skeletal nanoparticles either through cross-metathesis or a newly described stitching mechanism. After solvent exchange and drying with supercritical fluid CO_2 into aerogels (bulk densities in the range 0.27−0.63 g cm^{-3}, versus 0.20 g cm^{-3} of the native network), the bridging nature of the polymer is inferred by a >10-fold increase in mechanical strength and a 4-fold increase in the energy absorption capability relative to the native samples. The cross-linking polymer was freed from silica by treatment with HF, and it was found by GPC that it consists of a long and a short component, with around 400 and 10 monomer units, respectively. No evidence (by SAXS) was found for the polymer coiling up into particles, consistent with the microscopic similarity (by SEM) of both native and cross-linked samples. Most importantly, the polymer does not need to spill over higher aggregates for greatly improved mechanical strength; mechanical properties begin improving after the polymer coats primary particles. Extremely robust materials are obtained when the polymer fills most of the fractal space within secondary particles.

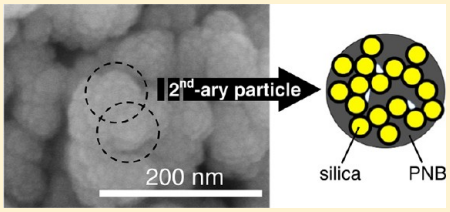

KEYWORDS: *silica, aerogel, cross-linking, mechanism, ROMP, norbornene, polymer, hierarchical, primary particles, secondary particles, SANS, SAXS, rheology*

1. INTRODUCTION

Low-density, open-cell, nanoporous solids consisting of three-dimensional (3D) assemblies of nanoparticles are referred to as aerogels and have been pursued for their bulk properties, such as high surface areas, low thermal conductivities, low dielectric constants, and high acoustic attenuations.[1] The most well-studied of those materials are silica aerogels; they are synthesized either by an acid-catalyzed gelation of aqueous sodium silicate solutions[2] or by acid- or base-catalyzed hydrolysis and polycondensation of silicon alkoxides into wet-gels that subsequently are dried by converting the pore-filling solvent into a supercritical fluid (SCF) that is vented off isothermally.[1] Conveniently, prior to the SCF drying, gelation solvents are extracted in an autoclave with liquid CO_2 whose low critical point (31.1 °C, 7.38 MPa) renders the process safer.

The most serious impediment against the practical (commercial) use of aerogels has been poor mechanical strength.[1] That issue was addressed successfully 10 years ago, by using the innate surface functionality of silica (−OH groups) for the covalent postgelation anchoring and accumulation of a polymer coating on the nanoscopic skeletal framework. The mechanical properties of the composite improved dramatically over those of the native silica framework while most of the porosity and, therefore, the desirable bulk aerogel properties, were preserved.[3] This process has been referred to as cross-linking and has been extended to over 30 different metal and semimetal

Received: June 7, 2012
Revised: July 30, 2012
Published: August 23, 2012

aerogels in addition to silica.[4] The mechanical strength-to-weight ratio of such polymer-cross-linked aerogels far surpasses not only that of native aerogels but also that of other materials considered strong.[5] Selected polymer cross-linked networks are strong enough to withstand stresses during ambient pressure drying from low vapor pressure solvents, for example, pentane.[6] Others are suitable for applications typically unrelated to aerogels, for example, in ballistic protection (armor).[3c] Further, as suggested by a recent quantitative (100% efficient) conversion of polyacrylonitrile-cross-linked silica aerogels to isomorphic SiC aerogels,[7] emerging applications include the carbothermal synthesis of a wide array of monolithic, highly porous metals and ceramics.

The cross-linking process is akin to grafting polymers onto surfaces. It has been demonstrated with both grafting-to and grafting-from methods. Generally, both require a modification of the skeletal nanoparticles by cogelation of tetramethyl orthosilicate (TMOS) with a trialkoxy silane derivative of the modifier.[8] In grafting-from cross-linking, polymerization begins at the surface of the skeletal nanoparticles, which are modified either with free radical,[9] atom transfer radical,[10] or anionic polymerization initiators. This process has been conducted both in the wet-gel state with polystyrene, polymethylmethacrylate, and polyacrylonitrile and in the dry aerogel state by the vapor deposition of suitable monomers (e.g., cyanoacrylates).[11] Grafting-to has been more versatile. It is based on solution polymerization of monomers in the pores that engages the surface functional groups. It includes aerogels cross-linked with isocyanate-derived polyurea using for backbone attachment either the innate hydroxyl surface functionality of silica[12] or amine-modified silica obtained by cogelation of TMOS with 3-aminopropyltriethoxysilane (APTES).[13] Amine-modified silica has also been used for cross-linking with epoxides.[14] A reaction of dangling amine groups with chloromethylstyrene has led to cross-linking with polystyrene.[15] Cross-linking with polystyrene has also been successfully conducted by a direct surface modification with olefins via cogelation of TMOS with vinyltrimethoxysilane.[16]

Despite the rather intense activity in this area, the nature of cross-linking at the fundamental building block level (primary and secondary nanoparticles) has remained ambiguous. As inferred by SEM, the microstructure is not affected visibly by the cross-linking process. Hence, the cross-linkng polymer has been assumed to follow the contour surface of the skeletal framework and, therefore, has been referred to as conformal. However, the exact location of the polymer on the backbone is important for correlating nanostructure with bulk material properties, such as porosity, surface area, and mechanical strength, and also for the synthesis of new porous materials that rely on intimate contact of skeletal inorganic nanoparticles with, for example, a carbonizable polymer.

Specifically, a first key question to be answered addresses the amount of polymer required for maximum mechanical strength with a minimum penalty in surface area, density, and porosity. In addition, noting that interpenetrating organic/inorganic networks in the much more compact xerogel form react carbothermally toward metals and carbides much more efficiently (at up to 400 °C lower temperatures) than aerogels,[17] it is expected that core–shell structures, such as polymer cross-linked aerogels, would be more attractive than interpenetrating networks, and therefore knowledge of the exact location of the polymer is also key.

That investigation must rely on a polymerization process yielding a rather well-defined, soluble polymer that can be readily washed off if unbound. For this, we turned to cross-linking of silica aerogels with norbornene by ring-opening metathesis polymerization (ROMP).[18] ROMP-derived polymers, such as both polynorbornene and polydicyclopentadiene, are extremely robust, use inexpensive monomers, and have been commercially successful. ROMP-derived all-organic aerogels have also been recently described.[19] Closer to our purposes, ROMP has been used in the surface-initiated mode by immobilizing suitable catalysts on surfaces to produce, in a grafting-from fashion, polymeric thin films,[20] polymer brushes,[21] and core–shell type structures on both silica and gold.[22] Our process, however, was related to grafting-to ROMP. The latter has been used with carbon nanotubes (CNTs) functionalized with norbornene to produce both CNT/polydicyclopentadiene composites[23] and surface-grafted polymer supports.[24]

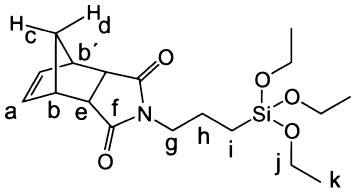

Si-NAD

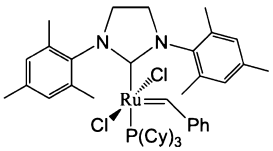

GC-II

Here, the norbornene functionality on the pore surfaces of silica aerogels was provided by a cogelation of TMOS with a new norbornene derivative, **Si-NAD**. The pores were filled with a norbornene (NB) solution. ROMP was then conducted at room temperature using a water-tolerant, second generation Grubbs' catalyst (**GC-II**). Unbound polynorbornene was washed off during typical solvent exchanges. Probing the location of the polymer was a complex issue; no single characterization method was sufficient to address by itself. Hence, the nanostructure was probed chemically both at the molecular level by IR, ^{13}C, and ^{29}Si solids NMR and at the nanoscopic level by SAXS, SANS, TEM, and SEM. Porosity was investigated using N_2 sorption. All results were correlated with the macroscopic mechanical strength using quasi-static compression. Control materials included both the native (noncross-linked) NB-modified silica (**n-SiNAD**) which, in turn, was referenced against native TMOS-derived silica (**n-TMOS**), and silica obtained by a cogelation of TMOS with APTES (**n-TMOS-co-APTES**). Overall, the polymer first coated the primary particles. In that regard, a mild degree of cross-linking was sufficient for improving the mechanical properties to a level that silica aerogels are no longer fragile materials. Complete filling of the fractal space within the secondary particles is essential, however, for ultimate mechanical strength.

2. EXPERIMENTAL SECTION

2.a. Materials. All reagents and solvents were used as received, unless noted otherwise. Dicyclopentadiene was purchased from Fluka. Maleic acid, thionyl chloride, 3-aminopropyltriehoxysilane (APTES), tetramethylorthosilicate (TMOS), a 14.8 N ammonium hydroxide solution, norbornene, second generation Grubbs' catalyst **GC-II** ((1,3-bis(2,4,6-trimethylphenyl)-2-imidazolidinylidene) dichloro-(phenylmethylene) (tricyclo-hexylphosphine) ruthenium) and anhydrous toluene were purchased from Aldrich Chemical Co. HPLC grade tetrahydrofuran (THF) was purchased from Fisher and was distilled from lithium aluminum hydride. Cyclopentadiene was obtained via a reverse Diels–Alder reaction by distillation of dicyclopentadiene (bp 170 °C).[25] Nadic acid was synthesized according to literature procedures[25] by a Diels–Alder reaction between cyclopentadiene

dx.doi.org/10.1021/cm3017648 | Chem. Mater. 2012, 24, 3434–3448

and maleic acid (mp 182−186 °C; Sigma-Aldrich: *endo*-, 175 °C (dec.); *endo/exo*-, 185−189 °C).

*Synthesis of N-(3-Triethoxysilylpropyl)-5-norbornene-2,3-dicarboximide (**Si-NAD**).* The process is summarized in Scheme 1: nadic

Scheme 1. Synthesis of Si-NAD

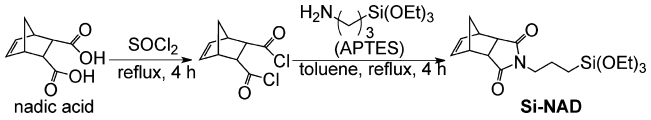

acid (7.8 g, 0.0428 mol) was added under magnetic stirring at room temperature to an excess of thionyl chloride (25.0 mL, 0.3441 mol) in a 2-neck round-bottom flask, and the mixture was refluxed for 4 h under N_2. At the end of the period, the reaction mixture was first allowed to cool to room temperature, the reflux apparatus was converted to a distillation setup, and the excess of thionyl chloride was removed under reduced pressure using an aspirator connected through a drying tube. The solid product was used without further purification. First, it was dissolved in anhydrous toluene (25 mL) added with a syringe through a septum at room temperature. Then, APTES (10.0 mL, 0.0428 mol) was added to the solution under N_2 with a syringe, and the mixture was refluxed for 4 h under magnetic stirring. At the end of the period, the reaction mixture was allowed to cool to room temperature and toluene was removed by distillation under reduced pressure, again using an aspirator connected through a drying tube, to yield a viscous liquid, which was further dried under vacuum to yield a waxy yellow solid of **Si-NAD**. Received 13.0 g (75%); mp 40−45 °C; ^{1}H NMR (400 MHz, $CDCl_3$) δ (ppm) 6.09 (dd, 2H, J_{ab} = 4.00 Hz, $J_{ab'}$ = 2.00 Hz, H_a), 3.80 (q, 6H, J_{jk} = 6.80 Hz, H_j), 3.36−3.40 (m, 2H, H_b), 3.32 (t, 2H, J_{gh} = 7.40 Hz, H_g), 3.23 (dd, 2H, J_{eb} = 3.00 Hz, $J_{eb'}$ = 1.40 Hz, H_e), 1.73 (dt, 1H, J_{cd} = 8.40 Hz, J_{cb} = 1.40 Hz, H_c), 1.50−1.58 (m, 3H, H_d and H_h), 1.21 (t, 9H, J_{kj} = 6.80 Hz, H_k), 0.50−0.60 (m, 2H, H_i); ^{13}C NMR (100 MHz, $CDCl_3$) δ (ppm) 177.9, 134.6, 58.6, 52.4, 45.9, 45.1, 41.2, 21.5, 18.5, 8.1; ^{29}Si NMR (79.415 MHz, $CDCl_3$) δ (ppm) −46.26. HRMS calcd for $C_{18}H_{29}NO_5SiNa^+$, 390.17072; found, 390.17045. **Si-NAD** is moisture-sensitive, and to increase its shelf life, facilitate handling, and standardize the procedure, it was stored as a 0.5 M solution in dry THF under N_2 at 10 °C.

*Preparation of Native Silica Aerogels Incorporating **Si-NAD** (**n-SiNAD**).* Native silica aerogels were formulated with 10% mol/mol of silicon coming from **Si-NAD** (the balance from TMOS). The stock solution of **Si-NAD** in THF (0.5 M) was allowed to warm to room temperature, and an aliquot (5.2 mL, 0.0026 mol) was transferred into a round-bottom flask. The solvent was removed at 40 °C under reduced pressure, and the resulting viscous liquid was dissolved in a mixture of methanol (4.5 mL) and TMOS (3.45 mL, 0.0235 mol) (Solution A). A second solution (Solution B) consisting of methanol (4.5 mL), distilled water (1.5 mL), and 80 μL of 14.8 N aq NH_4OH was added to Solution A, and the resulting sol was shaken vigorously for 30 s and was poured either into polypropylene molds (Wheaton polypropylene OmniVials, Part No. 225402, 1 cm in diameter) or into 10 cm^3 polyethylene syringes (Nonsterile BD Luer-Lok Tip, Part No. 301029, 14 mm in diameter). The latter molds were used for samples intended for compression testing. All sols gelled within 10−15 min at room temperature. The resulting wet-gels were aged in their molds for 24 h at room temperature and solvent-exchanged first with THF and then with acetone using four washes per solvent, 8 h per wash cycle, and 4× the volume of the gel for each wash. Acetone-filled wet-gels were dried in an autoclave to native aerogels with liquid CO_2, which was removed at the end as a SCF.

*Preparation of Norbornene-Cross-Linked Silica Aerogels (**X-SiNAD**).* THF-filled wet-gels (see above) were equilibrated for 24 h at room temperature in 10% w/w (0.93 M), 20% w/w (1.83 M), or 30% w/w (2.71 M) solutions of norbornene in THF with frequent swirling. The volume of each norbornene solution was four times the volume of each gel. Subsequently, wet-gels together with the surrounding norbornene solutions were cooled in a freezer for 2 h at −5 °C. A THF solution of the Grubbs' catalyst **GC-II** (1.0 mL, containing 0.025, 0.020 or 0.015% mol/mol relative to the amount of NB in the 10%, 20%, or 30% cross-linking solutions, respectively) was added to the cold monomer solution, and the vials were immediately placed back in a freezer for equilibration over another 12 h with intermittent swirling. At the end of that period, the wet-gels in the monomer/**GC-II** solutions were allowed to warm to room temperature. As the temperature increased, the monomer solution began to build up viscosity. The wet-gels were taken out of the viscous polymer solution just before it gelled (0.5 to 2 h), the remaining viscous liquid on the surface of the gels was wiped off with a Kimwipe tissue (Kimberly-Clark), and the wet-gels were placed in tightly closed vials (20 mL) with a small amount of THF to keep the environment inside saturated with THF vapors. After 4 h, wet-gels were washed with THF (four washes, 8 h per wash, using 4× the gel volume per wash) to remove loose polymer. Subsequently, wet-gels were solvent-exchanged with acetone (four washes, 8 h per wash cycle, using 4× the gel volume per wash) and dried in an autoclave with CO_2 to yield **X-SiNAD**. Meanwhile, the viscous cross-linking solution surrounding the silica wet-gels was left by itself to gel, and the polymer gel was aged in parallel with the cross-linked wet silica gels for 4 h. At the end of the period, the polymer was dissolved in a large excess of THF, precipitated with methanol, and analyzed by modulated differential scanning calorimetry and gel permeation chromatography (see Methods section below).

Control native silica and amine-modified silica aerogels were prepared according to literature procedures: for native silica aerogels (**n-TMOS**), Solution A consisting of 3.85 mL of TMOS (0.0261 mol) and 4.5 mL of CH_3OH was mixed at room temperature with Solution B consisting of 4.5 mL of CH_3OH, 1.5 mL of H_2O, and 40 μL of concentrated aqueous NH_4OH;[26] for native amine-modified silica aerogels (**n-TMOS-co-APTES**), Solution A consisting of 2.887 mL of TMOS (0.0196 mol), 0.963 mL of APTES (0.0041 mol), and 4.5 mL of CH_3CN was cooled in dry ice/acetone and mixed with a similarly cold Solution B consisting of 4.5 mL of CH_3CN and 1.5 mL of H_2O.[13a] The sol was poured into molds to gel. Wet **n-TMOS** silica gels were washed once with CH_3OH and 4× with acetone and dried with CO_2 taken out as a SCF. Wet, amine-modified silica gels (**n-TMOS-co-APTES**) were washed 4× with CH_3CN and were dried with CO_2 taken out again as a SCF.

2.b. Methods. Supercritical fluid CO_2 drying was conducted using an autoclave (SPI-DRY Jumbo Supercritical Point Dryer, SPI Supplies, Inc., West Chester, PA). Bulk densities (ρ_b) were calculated from the weight and the physical dimensions of the samples. Skeletal densities (ρ_s) were determined using helium pychnometry with a Micromeritics AccuPyc II 1340 instrument. Porosities, Π, were determined from ρ_b and ρ_s. Surface areas and pore size distributions were measured by nitrogen sorption porosimetry using a Micromeritics ASAP 2020 surface area and porosity analyzer. In preparation for surface area and skeletal density determination, samples were outgassed for 24 h under vacuum at 80 °C. (A separate series of samples was also outgassed at 50 °C in order to remain below the glass transition temperature of the polymer. Data were practically identical for samples outgassed at either temperature.) Average pore diameters were determined by the $4 \times V_{Total}/\sigma$ method, where V_{Total} is the total pore volume per gram of sample and σ the surface area determined by the Brunauer−Emmett−Teller (BET) method from the N_2 adsorption isotherm. The value of V_{Total} can be calculated either from the single highest volume of N_2 adsorbed along the adsorption isotherm or from the relationship $V_{Total} = (1/\rho_b) - (1/\rho_s)$. Average pore diameter values were calculated by both methods and are cited herewith; if those values converge, it is considered as indication that the material is mesoporous. If average pore diameters calculated using $V_{Total} = (1/\rho_b) - (1/\rho_s)$ are significantly higher, that is taken as evidence for macroporosity.

Liquid ^{1}H, ^{13}C, and ^{29}Si NMR were recorded with a 400 MHz Varian Unity Inova NMR instrument (100 MHz carbon frequency and 79.415 MHz silicon frequency).

High resolution, accurate mass analysis was conducted by direct infusion electrospray ionization (ESI) mass spectrometry using an LTQ OrbitrapXL hybrid mass spectrometer (Thermo Scientific,

dx.doi.org/10.1021/cm3017648 | *Chem. Mater.* 2012, 24, 3434−3448

San Jose, CA). Using the on-board syringe pump, a THF sample of **Si-NAD**, diluted in methanol, was infused into the source at a flow rate of 5 μL min^{-1}. The ESI voltage was 5 kV, the sheath gas flow rate was 8 (arbitrary units in the software), and the capillary temperature was 275 °C. Mass analysis was done in the Orbitrap FT mass analyzer with resolution set to 100 000. One hundred sixty four (164) individual scans were acquired and averaged.

Chemical characterization of native and cross-linked silica aerogels was conducted with infrared (IR) and solid-state ^{13}C NMR spectroscopy. IR spectra were obtained in KBr pellets with a Nicolet-FTIR Model 750 Spectrometer. Solid-state ^{13}C NMR spectra were obtained with samples ground into fine powders on a Bruker Avance 300 Spectrometer with a 75.475 MHz carbon frequency using magic angle spinning (at 7 kHz) with broadband proton suppression and the CPMAS TOSS pulse sequence for spin sideband suppression.

Thermogravimetric analysis (TGA) was conducted in air with a TA Instruments model Hi-Res-TGA 2950 analyzer at a heating rate of 10 °C min^{-1}.

Modulated differential scanning calorimetry (MDSC) was conducted under N_2 with a TA Instruments Differential Scanning Calorimeter Model Q2000 at a heating rate of 10 °C min^{-1} in the modulated T4P mode, using 60 s as the modulation period and 1 °C as the modulation amplitude. Samples were subjected to two heating scans and one cooling scan from 0 to 280 °C. Glass transition temperatures were determined from the second heating scan.

The structure of the fundamental building blocks of the materials was probed with both small-angle X-ray scattering (SAXS) and small-angle neutron scattering (SANS), using 2−3 mm-thick disks, 0.7−1.0 cm in diameter. SAXS was carried out with a PANalytical X'PertPro Multipurpose Diffractometer (MPD) configured for SAXS, using Cu Kα radiation (λ = 1.54 Å) and a 1/32° SAXS slit together with a 1/16° antiscatter slit on the incident beam side and 0.1 mm antiscatter slit and Ni 0.125 mm automatic beam attenuator on the diffracted beam side. Samples were placed in circular holders between thin Mylar sheets, and scattering intensities were measured with a point detector in the transmission geometry by 2θ scans ranging from −0.1 up to 5°. SANS was conducted with a time-of-flight, low-Q diffractometer (LQD) at the Manuel Lujan, Jr., Scattering Center of the Los Alamos National Laboratory.[27] SANS scattering data were recorded in absolute units (cm^{-1}), while SAXS data are reported in arbitrary units as a function of Q, the momentum transferred during a scattering event. Data analysis was conducted with the Irena SAS tool for modeling and analysis of small angle scattering within the commercial Igor Pro software package (WaveMetrics, Inc. Lake Oswego, OR).[28]

Scanning electron microscopy (FESEM) was conducted with samples coated with Au using a Hitachi S-4700 field emission microscope. Transmission electron microscopy (TEM) was conducted with a FEI Tecnai F20 instrument employing a Schottky field emission filament operating at a 200 kV accelerating voltage. For TEM, samples were ground to fine powder by hand in a mortar with a pestle and the smallest particles were selected and placed on a 200 mesh copper grid bearing a lacey Formvar/carbon film for microscopy. At least six different areas/particles were examined on each sample to ensure that the results were representative of the material.

For molecular weight determinations of polynorbornene, **X-SiNAD-(xx)** samples were ground to coarse powders, ~0.5 g of which was treated with 5 mL of an aqueous HF solution (1 M) for 1 h, with intermittent vigorous mixing. The polymer was extracted in chloroform by multiple washes, chloroform extracts were combined, the solvent was removed at 40 °C under reduced pressure, and the polymer was further dried in a vacuum oven at 40 °C for 12 h. The residue was dissolved in THF and was analyzed by gel permeation chromatography (GPC) using a Shodex GPC KH-803 L column connected to a Shimadzu liquid chromatograph (LC-10AD) equipped with a UV−vis detector (SPD-10AV). HPLC grade THF was used as eluent at 1 mL min^{-1}. Linear polystyrene standards from Varian (Polystyrene Low EasiVials; Part Nos. PL2010-0400 and PL2010-0403) were used for calibration. Multiple Gaussian curves were fitted within the experimental chromatograms using OriginLab's data analysis and graphing software version OriginPro 8. Number- and weight-average molecular weights (M_n and M_w, respectively) and polydispersity indexes (M_w/M_n) were calculated using the fitted chromatograms.[29]

Compression testing was performed according to the ASTM D695-02a standard on cylindrical specimens using a Instron 4469 universal testing machine frame. According to the ASTM standard, the height-to-diameter ratio of the specimen was 2:1; typical samples were machined to about 2.0 cm in length and 1.0 cm in diameter.

The rheological behavior of TMOS and TMOS/**Si-NAD** sols was recorded with a TA Instruments AR 2000ex Rheometer using an aluminum cone (60 mm diameter, 2° angle) and a Peltier plate geometry with a 1 mm gap between them. The instrument was operated in the continuous oscillation mode, and time-sweep experiments were performed with a fixed strain amplitude either from the beginning (case of TMOS) or 10 min after mixing of Solution A with Solution B (case of TMOS/**Si-NAD**), until gelation. The Peltier plate was set at 20 °C. The gel point was determined using a dynamic multiwave method with three superimposed harmonics with frequencies 1, 4, and 8 rad s^{-1}. The strain of the fundamental oscillation (1 rad s^{-1}) was set at 5%.

The relative rates of incorporation of TMOS and **Si-NAD** in the **n-SiNAD** gel network were determined using liquid ^{29}Si NMR on the 400 MHz Varian Unity Inova NMR instrument. A Teflon liner inside a 5 mm glass tube was used as sample holder. The field-frequency was locked to deuterium (CD_3OD). Broad-band proton decoupling was applied to suppress possible nuclear Overhauser effects. Chromium acetylacetonate (0.015 M) and tetramethylsilane (TMS) were added in the sol to reduce the spin−lattice relaxation time and as an internal standard, respectively. Spectra were collected in regular intervals during gelation and beyond, using 256 scans and a relaxation delay of 1 s. A receiver gating time of 500 μs following a pulse of 7.8 μs was also applied in order to eliminate the broad background signal from the borosilicate glass in the NMR tube and probe.

3. RESULTS AND DISCUSSION

3.a. Synthesis and Characterization of Native n-SiNAD Aerogels. The monomer **Si-NAD** can be considered an APTES derivative. Like the latter, **Si-NAD** does not gel by itself.[13−15] Thus, in both, in analogy to APTES and as summarized in Scheme 2, silica wet-gels and aerogels incorporating norbornyl moieties were prepared by replacing 10 mol % of the TMOS with **Si-NAD** from a typical NH_4OH-catalyzed TMOS-gelation process. Extensive prior work with APTES-modified silica has relied on a 17.3 mol % APTES.[13−15] Here, however, it was deemed appropriate to use a lower **Si-NAD**:TMOS mol ratio in order to capture cross-linked materials at earlier stages of cross-linking and thus explore the evolution of mechanical properties closer to the native network.

The cogelation of **Si-NAD** with TMOS was followed in comparison with the gelation of TMOS with itself. That was accomplished by monitoring both the rheological properties of the sol as well as the ^{29}Si NMR signal of the monomers. Figure 1A shows the typical evolution of the storage (G') and the loss (G'') modulii of the sol as a function of time from mixing the sol. These curves cross, as expected, near the gelation point, where the elastic properties of the newly formed, rigid gel become dominant. (For corresponding data regarding gelation of TMOS only, refer to Figure S.1 in Supporting Information.) The actual gelation point (a physical property of the system) is given by the inflection point of the tan δ (=G''/G') versus time plot at a given frequency (included in Figure 1A). This point can alternatively be given as the common (independent of frequency) crossing point of all tan δ versus time curves (Figure 1B).[30] This common crossing point is also located at the minimum of the statistical variable $\log(s/\langle\tan\delta\rangle)$ versus time-after-mixing plot (see inset in Figure 1B; s is the standard deviation of the three tan δ obtained at specified times during gelation, at three different

dx.doi.org/10.1021/cm3017648 | Chem. Mater. 2012, 24, 3434−3448

Scheme 2. Preparation of Both Native and Cross-Linked Aerogels Incorporating Si-NAD

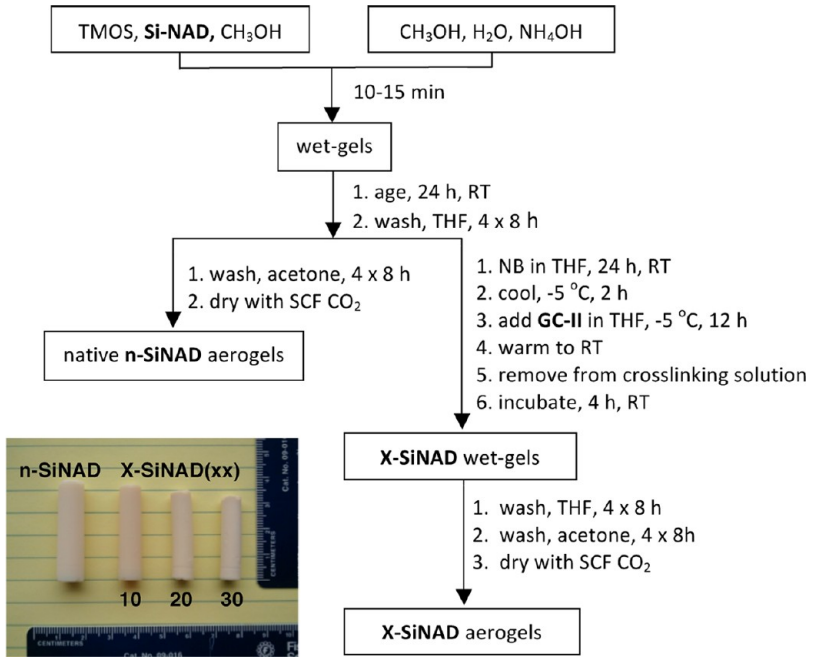

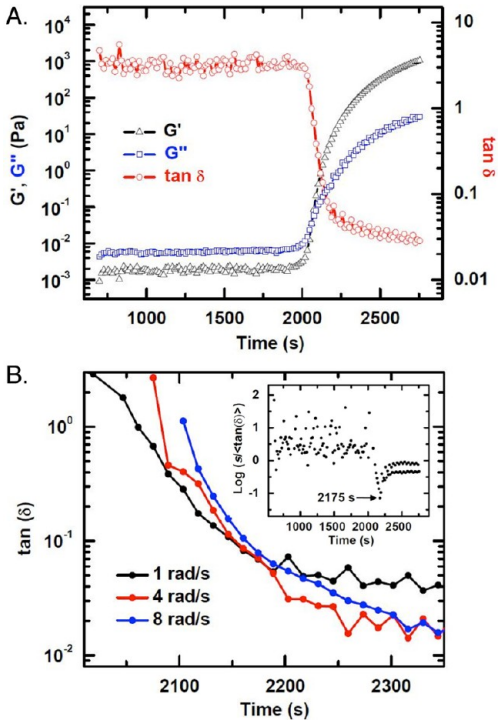

Figure 1. Rheology during the base-catalyzed (NH_4OH, 40 μL) cogelation of **Si-NAD** with TMOS (1:9 mol/mol) at 20 °C, according to the procedure described in the Experimental Section. A. Evolution of the storage (G') and loss (G'') modulii as well as of tan δ versus time from mixing the sol. Data shown at 1 rad s^{-1} oscillation frequency. (For other parameters, see Experimental Section) B. tan δ versus time from mixing the sol, close to the gelation point, at three different oscillation frequencies. Inset: Statistical variable versus time (see text). The gelation point is defined at the minimum.

oscillatory frequencies of the cone, operated in the multiwave mode).[31] Results are summarized in Table 1. At equal catalyst concentrations, TMOS gels faster than the TMOS/**Si-NAD** system, suggesting that **Si-NAD** interferes with the gelation of TMOS. At the gelation point, the tan δ value is related to the gel relaxation exponent "n" via eq 1.[32]

$$\tan \delta = \tan(n\pi/2) \quad (1)$$

In turn, considering the excluded volume of the (primary) particles forming the clusters, "n" is related via eq 2 to the fractal dimension, D_f, of the clusters existing at the gel point (for three-dimensional nonfractal clusters, $D = 3$).[33]

$$n = \frac{D(D + 2 - 2D_f)}{2(D + 2 - D_f)} \quad (2)$$

At two different catalyst concentrations and, therefore, different gelation times, the D_f values calculated via eq 2 for the native **n-SiNAD** gels are in the [2,3] interval suggesting a reaction-limited cluster–cluster aggregation mechanism for network formation.[34] Additionally, the D_f values of **n-SiNAD** are sufficiently close to those of **n-TMOS** gels (Table 1), suggesting that the space filling pattern in the two types of wet-gels is similar.

A preeminent tool for the elucidation of the sol–gel chemistry of silicon alkoxides is ^{29}Si NMR.[35] Here (Figure 2A), the ^{29}Si signal is not lost after gelation. Additionally, the transient

Table 1. Rheological Data for the Gelation of TMOS and of TMOS/Si-NAD

alkoxide catalyst amount[a]	gelation point, t_g[b] (s)	tan δ at t_g	n[c]	D_f[d]
TMOS				
40 μL	690	0.33	0.203	2.32
TMOS/Si-NAD				
40 μL	2175	0.06	0.038	2.47
80 μL[e]	355	0.20	0.126	2.39

[a]All other parameters remaining the same as in the basic formulation described in the Experimental Section. [b]Identified at the minimum of the statistical function as shown in Figure 1B, inset. [c]From eq 1. [d]From eq 2. [e]Actual amount of catalyst used in gel synthesis, as described in the Experimental Section.

dx.doi.org/10.1021/cm3017648 | Chem. Mater. 2012, 24, 3434–3448

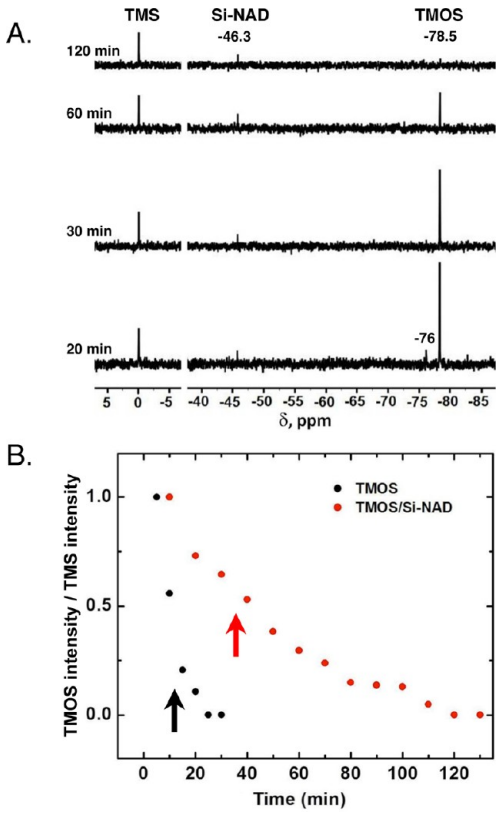

Figure 2. A. Liquid ^{29}Si NMR of a **Si-NAD**/TMOS sol (using 40 μL catalyst; see Experimental Section) as a function of time from mixing. (Solution stops flowing at ~25 min from mixing; formal gelation point by rheology at 36.25 min.) B. Comparative loss of TMOS signal (−78.5 ppm) in a TMOS versus a **Si-NAD**/TMOS sol at the same catalyst concentration. Arrows mark respective gelation points.

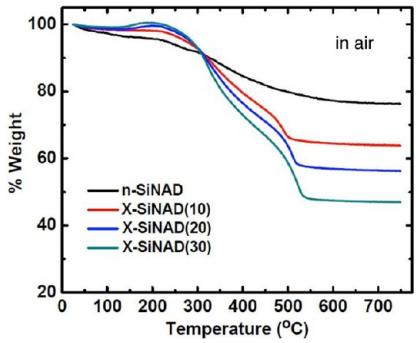

Figure 3. Thermogravimetric analysis (TGA) in air of samples as shown. The increase in mass at ~200 °C is attributed to the initial epoxidation of backbone double bonds.

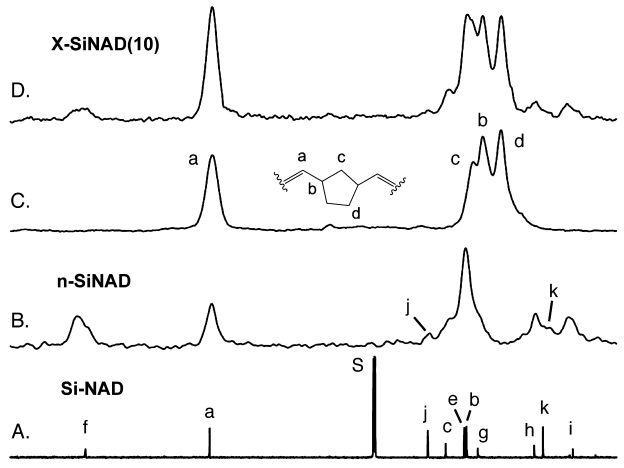

Figure 4. ^{13}C CPMAS NMR of solids samples, in comparison to the liquid ^{13}C NMR of **Si-NAD** ($CDCl_3$). Polynorbornene (frame C) was isolated from the cross-linking bath. For peak assignments, see structures in text.

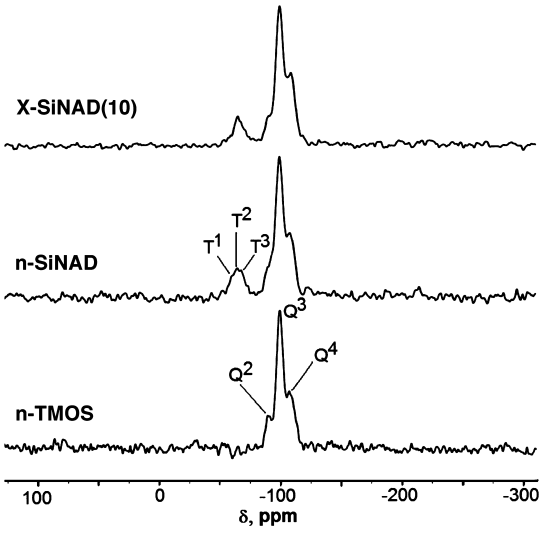

Figure 5. Solid ^{29}Si CPMAS NMR data.

appearance of a resonance peak at −76 ppm corresponds to hydrolysis products from TMOS $[(MeO)_{4-x}Si\text{-}(OH)_x]$.[35] That resonance disappears after gelation, in contrast to the TMOS resonance (−78.52 ppm) that remains present and keeps decreasing. Overall, it is noted that (a) a significant amount of TMOS is still unreacted at the gel point, when nanoparticles reach their bond-percolation threshold;[36] (b) **Si-NAD** (at −46.26 ppm) is still in the pores after all of the signal from TMOS is gone; and (c) in the absence of **Si-NAD**, TMOS is incorporated in the gel framework faster (see Figure 2B). Eventually, both TMOS and **Si-NAD** are incorporated in the network: (a) TGA in the air (Figure 3) shows that **n-SiNAD** leaves a ~76% w/w residue, versus 75.4% expected stoichiometrically if all **Si-NAD** is incorporated in the network with all alkoxides hydrolyzed; (b) the solids CPMAS ^{13}C NMR of **n-SiNAD** aerogels (Figure 4) is dominated by the $-(CH_2)_3-$NAD moiety, showing only very small residual signals from the ethoxy groups (peaks marked "j" and "k"); and finally, (c) the solids ^{29}Si NMR of **n-SiNAD** (Figure 5) shows both the Q and the T resonances expected from TMOS and **Si-NAD**, respectively. The Q^1−Q^4 distribution of intensities in both **n-TMOS** and **n-SiNAD** aerogels is the same. The most intense signal is at −98.78 ppm, corresponding to the Q^3 silicon participating in three Si−O−Si bridges. That fact, together with the small amount of residual ethoxy groups in the ^{13}C NMR spectrum, supports further that almost all of the original Si-OR groups have been hydrolyzed, and most have been incorporated into the silica network in the form of Si−O−Si bridges, while some remain as dangling OHs, a fact supported by the OH stretches in the IR spectra of all samples (see Figure S.2 in Supporting Information).

Both the rheology and the liquid ^{29}Si NMR data considered together suggest that, in both cases, **n-TMOS** and **n-SiNAD**,

dx.doi.org/10.1021/cm3017648 | *Chem. Mater.* 2012, 24, 3434−3448

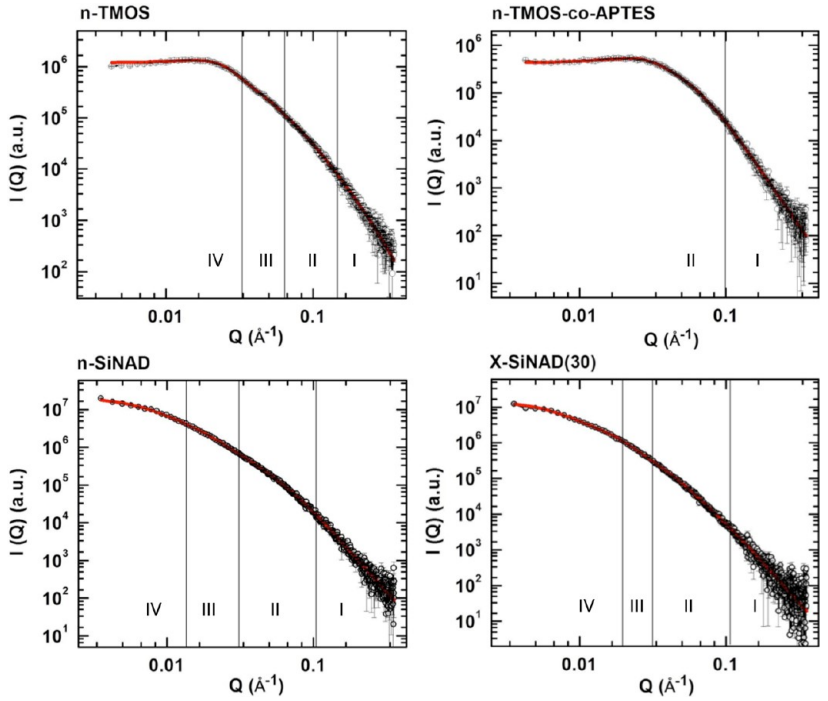

Figure 6. Small angle X-ray scattering (SAXS) data for aerogel samples. (Data are summarized in Table 2; for additional sample information, refer to Table 4.) Primary particle radii were extracted from Guinier Region II. Secondary particle radii from Region IV. Fractal dimensions of secondary particles from Region III. Fitting power-law Region I to modified Porod's law (eq 4) yielded the surface layer thickness of primary particles. **n-TMOS-co-APTES** did not yield information beyond the radius of primary particles (Region II) in the *Q*-range available.

the primary gel network was formed by TMOS. Presumably, either more TMOS or **Si-NAD** kept adding onto the network after its initial formation according to a monomer-cluster aggregation model. This conclusion is supported by the gradual and eventual disappearance of all ^{29}Si signals after gelation. That model also suggests that **Si-NAD** decorates the surfaces of the skeletal silica framework with NB, as intended, and agrees with previous speculation to that effect[3b] based on slower reaction rates expected from (a) ethoxy versus methoxy silanes and (b) alkyltrialkoxy versus tetraalkoxy silanes.[8,37] Within that monomer-cluster aggregation model, the slower gelation of the TMOS/**Si-NAD** system may be reconciled by assuming that elementary particles formed at early stages get partially capped with **Si-NAD**, which sterically hinders interparticle bond formation. However, Si−O−Si bridges are hydrolyzed off continuously and **Si-NAD** reprecipitates on the network during particle aggregation.

To gather further support for a TMOS-like network, we turned to small-angle X-ray scattering (SAXS), comparing native **n-SiNAD** with both **n-TMOS** and **n-TMOS-co-APTES** aerogels (Figure 6). Small angle neutron scattering (SANS) data when available agreed quite well with those from SAXS (see, for example, Figure S.3 in Supporting Information). That together with the high porosity of the samples suggests that all scattering information in SAXS arises from the particles, not from the pores. Results are summarized in Table 2. The high-*Q* region (Region I, Figure 6) of the **n-SiNAD** aerogels follows a power law, with a slope equal to 4.22 ± 0.03. The slopes for **n-TMOS** and **n-TMOS-co-APTES** aerogels are 3.97 ± 0.03 and 4.37 ± 0.02, respectively. At ∼4.0, the high-*Q* slope of **n-TMOS** indicates primary particles with abrupt interfaces. In **n-SiNAD** and **n-TMOS-co-APTES**, values > 4.0 indicate density-gradient (fuzzy) interfaces. The interfacial layer thickness, *t*, can be calculated via eq 3, assuming a Gaussian

$$t = (2\pi)^{0.5}s \tag{3}$$

distribution of matter at the nanoparticle interfaces with standard deviation *s*. In turn, *s* is obtained by fitting the scattering intensity to the suitably modified Porod's law (eq 4), whereas $I(Q)$ is the scattering intensity as a function of *Q*, *N* the number of scatterers per unit volume, $\Delta\rho$ the difference in scattering-length density between scatterers and the surrounding medium, and *S* the surface area of the scatterer.[38]

$$I(Q) = 2\pi N(\Delta\rho)^2 SQ^{-4}\exp[-s^2Q^2] \tag{4}$$

The surface layer thickness, *t*, was found equal to 3.8 ± 0.3 Å and 5.0 ± 0.3 Å for **n-TMOS-co-APTES** and **n-SiNAD**, respectively (Table 2). These values agree well with both the trend in the fully extended length of the $-(CH_2)_3NH_2$ group of APTES (3.86 Å) and of the $-(CH_2)_3$-NAD group of **Si-NAD** (8.09 Å), both by molecular modeling. The lower SAXS thickness of $-(CH_2)$-NAD implies some bending. The radius of the primary particles, R_1, is calculated via $R_g = 0.77 \times R$,[39] where R_g is the radius of gyration, obtained from the Guinier knee (Region II) in the log−log plot of $I(Q)$ versus *Q* of either the SAXS or the SANS data (Figure 6). The radii of the primary particles in **n-SiNAD** fall within the range of 7.1−7.7 nm and, therefore, are similar to those for **n-TMOS** (5.7 nm, by SAXS only, see Table 2). Both the presence and the size of primary particles in **n-SiNAD**, as inferred via SAXS, were both confirmed with TEM (Figure 7). Additionally, particles in the dimensions suggested by SAXS/TEM for primary particles are the smallest entities discernible in FESEM (Figure 8, whereas the primary particles are pointed at with arrows). Primary nanoparticles aggregated in 3D into mass fractal secondary particles with fractal dimension D_f are given by the slope of the second power-law region at lower *Q*-values (Region III,

dx.doi.org/10.1021/cm3017648 | *Chem. Mater.* 2012, 24, 3434−3448

Table 2. SAXS and SANS Data for Si-NAD Derived Aerogels and Controls (Native n-TMOS and n-TMOS-co-APTES)

	primary particles				secondary particles			
	high-Q slope[a]	thickness t[b] (Å)	$R_g(1)$[c] (nm)	R_1[d] (nm)	D_f[e]	$R_g(2)$[f] (nm)	R_2[d] (nm)	empty space[g] (% v/v)
				n-TMOS				
SAXS	3.97 ± 0.02	*h*	4.2 ± 0.1	5.5 ± 0.2	1.9 ± 0.3	17.6 ± 0.6	22.9 ± 0.8	85
				n-TMOS-co-APTES				
SAXS	4.37 ± 0.02	3.8 ± 0.3	3.97 ± 0.06	5.16 ± 0.08	*i*	*i*	*i*	
				n-SiNAD				
SAXS	4.22 ± 0.03	5.0 ± 0.3	5.94 ± 0.05	7.71 ± 0.06	2.07 ± 0.02	22.1 ± 0.2	28.7 ± 0.3	78
SANS	*j*	N/A	5.5 ± 0.2	7.1 ± 0.3	$2.07 \pm 0.00_2$	19.3 ± 0.5	25.1 ± 0.6	77
				X-SiNAD(10)				
SAXS	4.25 ± 0.05	6.0 ± 0.3	5.9 ± 0.1	7.7 ± 0.1	2.01 ± 0.03	16.1 ± 0.3	20.9 ± 0.4	70
SANS	*j*	N/A	5.5 ± 0.3	7.1 ± 0.4	1.93 ± 0.03	14.0 ± 0.4	18.2 ± 0.5	69
				X-SiNAD(20)				
SAXS	4.26 ± 0.04	6.8 ± 0.3	6.3 ± 0.2	8.2 ± 0.3	2.47 ± 0.02	16.5 ± 0.1	21.4 ± 0.1	70
SANS	*j*	N/A	5.2 ± 0.4	6.8 ± 0.5	$2.25 \pm 0.00_4$	12.5 ± 0.5	16.2 ± 0.6	67
				X-SiNAD(30)				
SAXS	4.30 ± 0.06	6.3 ± 0.5	7.2 ± 0.1	9.4 ± 0.1	1.55 ± 0.01	22.4 ± 0.3	29.1 ± 0.4	74
SANS	*j*	N/A	5.8 ± 0.2	7.5 ± 0.3	$0.82 \pm 0.00_2$	28.3 ± 5.0	$36._8 \pm 6._5$	83

[a]Referring to Figure 6: From power law Region I. [b]Via eq 3. [c]From Guinier Region II. [d]Particle radius = $R_g/0.77$. [e]From power law Region III. [f]From Guinier Region IV. [g]Within secondary particles. Calculated as described in Appendix I of Supporting Information. [h]Abrupt interface (Porod slope = 4.0). [i]No higher aggregates could be probed within the low-Q region accessible. [j]High-Q region not accessible.

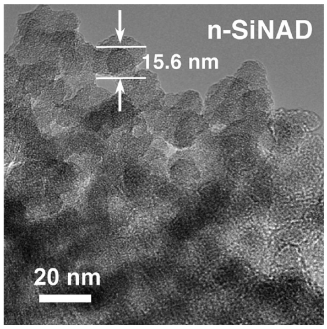

Figure 7. Transmission electron micrograph (TEM) of **n-SiNAD**. The primary particle diameter (15.6 nm) matches with that found using SAXS (15.4 nm; see Figure 6 and Table 2). For TEM of the **X-SiNAD(xx)** samples see Figure S.4 in Supporting Information.

Figure 6). D_f was found equal to 1.94 ± 0.28 for **n-TMOS** (by SAXS) and 2.07 ± 0.02 for **n-SiNAD** (both by SANS and SAXS; see Table 2). (It is noted that the aggregation of primary particles of **n-TMOS-co-APTES** with a radius of 5.16 nm was beyond the *Q*-range of our SAXS capability.) The radius of the secondary particles, R_2, was calculated again via the second radius of gyration, $R_g(2)$, which was obtained from the second Guinier knee (Region IV, Figure 6) by fitting the entire scattering profile according to the Beaucage Unified Model.[40] R_2 fell within the 25−29 nm range for **n-SiNAD** and ∼23 nm for **n-TMOS**. The secondary particles, by comparison with FESEM, are the entities enclosed by the *dark* dashed circles in Figure 8. The number of primary particles, $N(R_2)$, within the secondary particles can be calculated via eq 5, whereas $\zeta = \pi/3\sqrt{2} = 0.7405$ is the fill-factor in cubic or hexagonal closely

$$N(R_2) = \zeta\left(\frac{R_2}{R_1}\right)^{D_f} \quad (5)$$

packed spheres,[41] and R_1, R_2, and D_f have the same meaning as above. In turn, $N(R_2)$ can be used to calculate the percentage of empty space within secondary particles (see Appendix I in Supporting Information). Thus, with R_1 = 7.71 nm, R_2 = 28.7 nm, and D_f = 2.07, the secondary particles of **n-SiNAD** consist of 78% v/v empty space.

Finally, it is noted that the fractal dimensions of the secondary particles of both **n-SiNAD** and **n-TMOS** (2.07 ± 0.02 and 1.9 ± 0.3, respectively) are different (lower) than the fractal dimensions of the particles forming the gel network as identified by rheology (2.47 and 2.32, respectively, refer to Table 1). That difference strongly suggests that the gel network is not formed by secondary particles but by higher aggregates of the latter. That aggregation can be clearly seen in FESEM (entities enclosed by *white* dashed circles, Figure 8).

Overall, both neutron and X-ray scattering data further support a TMOS-derived fractal network of nanoparticles whose surface is decorated with NB moieties. That model is consistent with the macroscopic mechanical properties of the entire structure under quasi-static compression (Figure 9 and Table 3). Thus, while in terms of ultimate strength and within error **n-TMOS** and **n-SiNAD** aerogels behave similarly (ultimate compressive strengths at 3.3 ± 0.7 MPa versus 4.5 ± 0.4 MPa, respectively), suggesting a similar interparticle connectivity, on the other hand **n-SiNAD** are stiffer than **n-TMOS** (Young's modulii at 5.3 ± 0.3 MPa and 2.9 ± 0.3 MPa, respectively) consistent with a surface layer that gets on the way to bending of particles around their interparticle necks.[9] (It is also noted in passing that, in terms of ultimate strain, both native aerogels (**n-TMOS** and **n-SiNAD**) are capable of reaching unusually high values: ∼50% and ∼57%, respectively. Such supercompressibility for silica at those high densities has not previously been observed.[42] We speculate that this overlooked property of those materials is usually masked by macroscopic defects leading to premature failure. The matter is being investigated further.)

3.b. X-SiNAD Aerogels and the Topology of Cross-Linking. Scheme 3 summarizes the cross-linking process from a chemical perspective. ROMP initiated in the pores engages surface **Si-NAD** moieties. Interparticle bridging (cross-linking) should take place via either cross-metathesis or a stitching

dx.doi.org/10.1021/cm3017648 | *Chem. Mater.* 2012, 24, 3434−3448

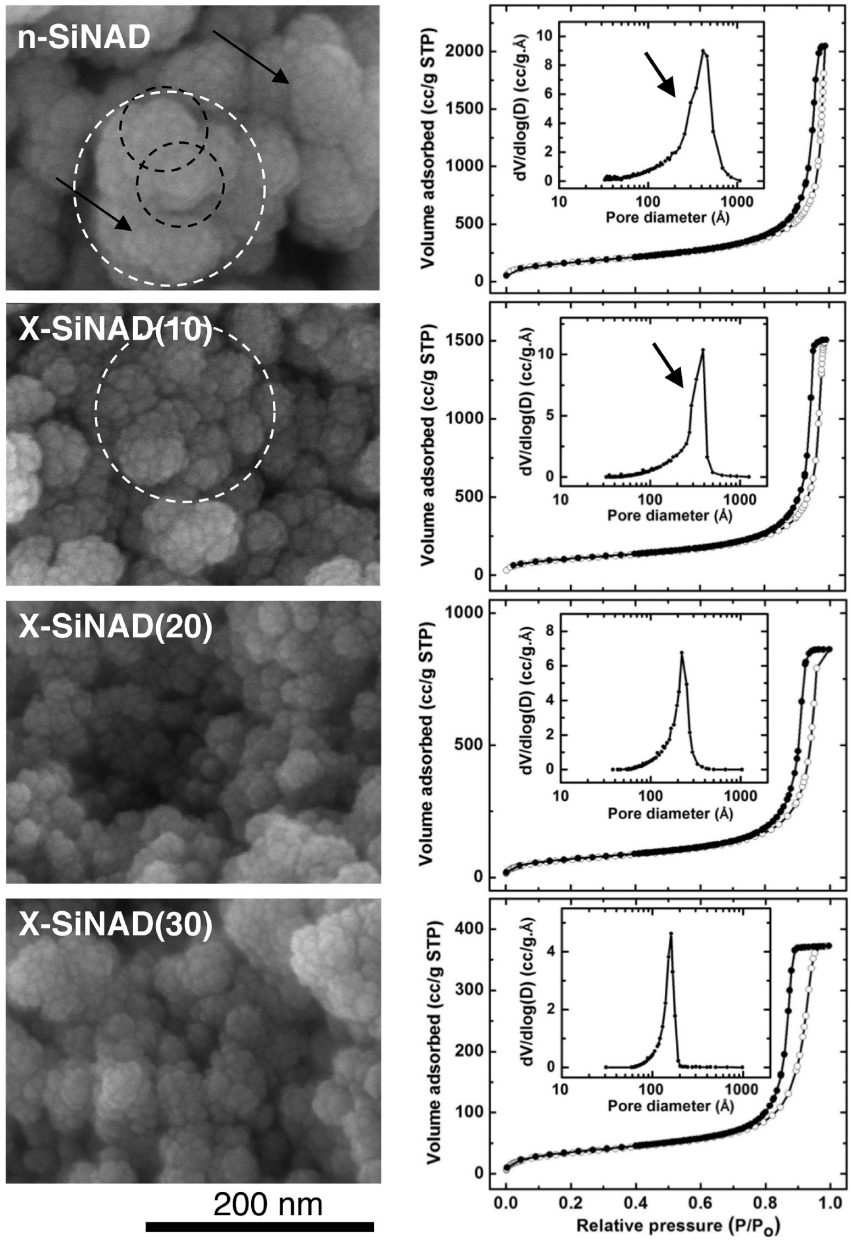

Figure 8. Scanning electron microscopy (SEM), N_2-sorption isotherms, and BJH plots (insets). Pertinent data, including bulk and skeletal densities, porosities, pore sizes, and pore size distributions are summarized in Table 4. In SEM, primary particles, as identified by both SAXS/SANS and TEM, are indicated with arrows. Dashed dark circles delineate secondary particles, as identified by SAXS/SANS. Dashed white circles delineate aggregates of secondary particles forming the network, as suggested by rheology. In BJH plots, arrows point at the low pore size shoulder that decreases in size, eventually disappearing as polymer uptake increases.

mechanism. Experimentally, the process was implemented as shown in Scheme 2. The pore-filling gelation solvent was first equilibrated with variable concentration solutions of NB in THF. A cold (−5 °C) THF solution of the **GC-II** catalyst was added to the also cold (−5 °C) NB bath surrounding the NB-equilibrated gels. Subsequently, samples were incubated at −5 °C to allow infusion of the catalyst into the gels without significant reaction, the criterion for which is increasing viscosity and ultimately gelation of the cross-linking bath itself. The cross-linking process was completed by allowing the system to warm-up to room temperature. Both short oligomers and loose polymer were removed using four THF washes according to procedures followed before.[3−8,12−17] Next, wet-gels were solvent-exchanged with acetone and dried in an autoclave with liquid CO_2 taken out supercritically. NB-cross-linked aerogels are referred to as **X-SiNAD(xx)**, where "xx" takes the values of 10, 20, or 30 denoting the weight percent concentration of NB in the cross-linking baths.

The ^{13}C NMR spectra of all **X-SiNAD(xx)** are dominated by polynorbornene (Figure 4). The ^{29}Si NMR spectra (Figure 5) are identical to that of native **n-SiNAD**, indicating no adverse effect by the cross-linking process upon the chemical makeup of the skeletal framework. General materials properties of **X-SiNAD(xx)** aerogels are summarized in Table 4. The polymer uptake by TGA (Figure 3) increases for more concentrated cross-linking solutions: from 16% to 26% and, ultimately, to 38% w/w, roughly in proportion to the monomer concentration in the cross-linking bath (Table 4). (For the calculation

dx.doi.org/10.1021/cm3017648 | *Chem. Mater.* 2012, 24, 3434−3448

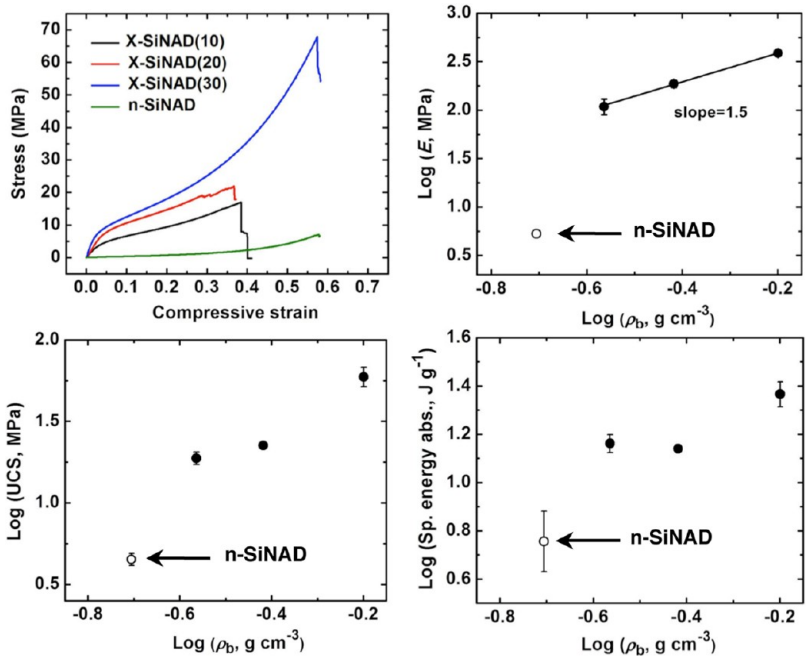

Figure 9. Mechanical characterization data under quasi-static compression (strain rate: 0.005 s^{-1}). In the log–log plots of Young's modulus (E), ultimate compressive strength (UCS) and specific energy absorption versus density, open circles show the corresponding property of the **n-SiNAD** network and dark circles those of the **X-SiNAD(xx)** samples. Results are summarized in Table 3.

Table 3. Quasi-Static Compression Data for Si-NAD Derived Aerogels and Controls (Native n-TMOS and n-TMOS-co-APTES)[a]

sample	bulk density, (ρ_b, g cm^{-3})	Young's Modulus, (E, MPa)	yield stress at 0.2% offset strain (MPa)	ultimate strength (MPa)	ultimate strain (%)	Poisson ratio	specific energy abs.[b] (J g^{-1})
n-TMOS	0.200	2.9 ± 0.3	0.13 ± 0.01	3.3 ± 0.7	49.7 ± 3.6		2.7 ± 0.6
n-TMOS-co-APTES	0.196	12.8 ± 1.5	0.37 ± 0.09	11.9 ± 6.8	60.8 ± 6.7		10.3 ± 4.7
n-SiNAD	0.197	5.3 ± 0.3	0.21 ± 0.02	4.5 ± 0.4	57.2 ± 5.8		5.7 ± 1.9
X-SiNAD(10)	0.273	108 ± 22	2.9 ± 0.4	18.8 ± 1.7	35.6 ± 3.2	0.08 ± 0.03	14.5 ± 1.3
X-SiNAD(20)	0.382	187 ± 18	5.6 ± 1.1	22.5 ± 0.1	39.0 ± 1.5	0.15 ± 0.02	13.8 ± 0.1
X-SiNAD(30)	0.632	386 ± 25	5.5 ± 0.9	59.3 ± 8.6	43.9 ± 5.9	0.27 ± 0.05	23.2 ± 2.9

[a]Average of three samples at strain rate = 0.005 s^{-1}. [b]Calculated from the area under the stress–strain curves at ultimate strain.

method of the weight percent of polymer from TGA data, see Appendix II in Supporting Information). Skeletal densities, ρ_s, decrease as the amount of polymer increases. However, the ρ_s values are also consistently lower than the ρ_s calculated from the skeletal densities of the native framework ($\rho_{\text{n-SiNAD}}$ = 1.811 g cm^{-3}, Table 4) and the density of free polynorbornene formed and isolated from the cross-linking bath (ρ_{PNB} = 1.129 g cm^{-3}, by He pycnometry). That discrepancy is attributed to closed pores (CP), whose volume fraction, V_{CP}, can be calculated via eq 6, and in turn be used to calculate the percent closed void

$$V_{CP} = \frac{1 - \left(\frac{f_{\text{n-SiNAD}}}{\rho_{\text{n-SiNAD}}} + \frac{f_{PNB}}{\rho_{PNB}}\right)\rho_{\text{X-SiNAD}}}{\rho_{\text{X-SiNAD}}} \quad (6)$$

space in the skeletal framework, ($f_{\text{n-SiNAD}}$ and f_{PNB} are the mass fractions of the skeletal framework and polymer, respectively.) The $\%V_{CP}$ values are cited in Table 4 and vary from 1.6% v/v in **X-SiNAD(10)** to 5.6% v/v in **X-SiNAD(30)**.

On the contrary, due to shrinkage, bulk densities, ρ_b, increased more than expected from simple polymer uptake. Native **n-SiNAD** shrank the least relative to the molds (6.0 ± 0.7% in linear dimensions), shrinking less than both **n-TMOS** and **n-TMOS-co-APTES** aerogels (8–13%). **X-SiNAD** shrank progressively more from 13 ± 1% [**X-SiNAD(10)**] to 27 ± 1% [**X-SiNAD(30)**] as the polymer content increased—see photograph in Scheme 2. The additional shrinkage of the X-samples is attributed to a pulling effect exerted by the polymer on the skeletal framework as it tries to contract in order to maximize its interstrand van der Waals forces. That additional shrinkage of the X-samples is taken as indirect evidence of bridging skeletal nanoparticles. The effect of shrinking is evident in FESEM (Figure 8): the microstructure of **n-SiNAD** includes larger voids in the macropore range (>50 nm). Those voids are not present in the X-samples, although the major morphostructural features of the native framework have been preserved. A more quantitative evaluation of the porous structure follows.

Open porosity, via $\Pi = 100 \times [(1/\rho_b) - (1/\rho_s)]/(1/\rho_b)$, decreased from approximately 89% in **n-SiNAD** to 55% v/v of void space in the most dense cross-linked samples. A more detailed evaluation of the porous structure was conducted with N_2-sorption porosimetry. Internal surface areas, σ, calculated by the BET method, applied on the early part of the adsorption isotherms (Figure 8), decreased as the polymer uptake increased

dx.doi.org/10.1021/cm3017648 | Chem. Mater. 2012, 24, 3434–3448

Scheme 3. Crosslinking Mechanisms[a]

A. Cross-metathesis

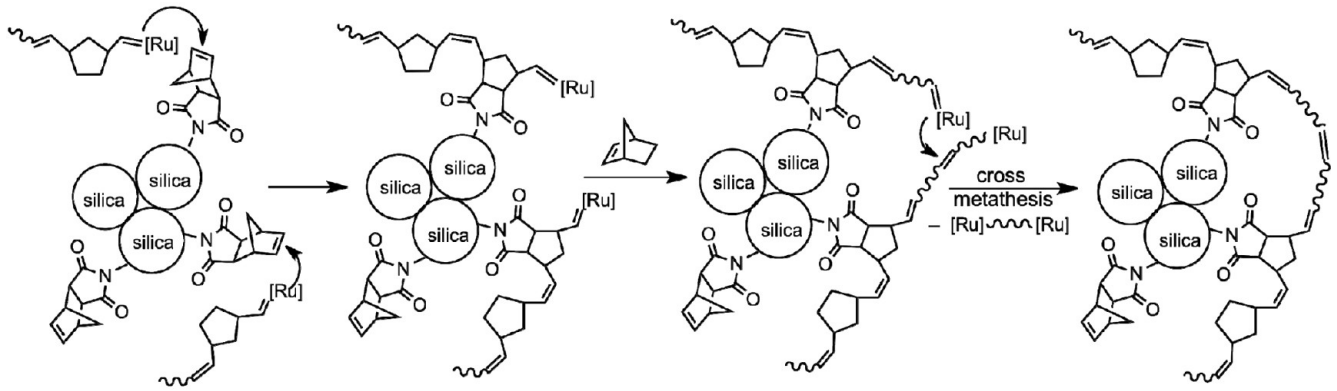

B. Stitching

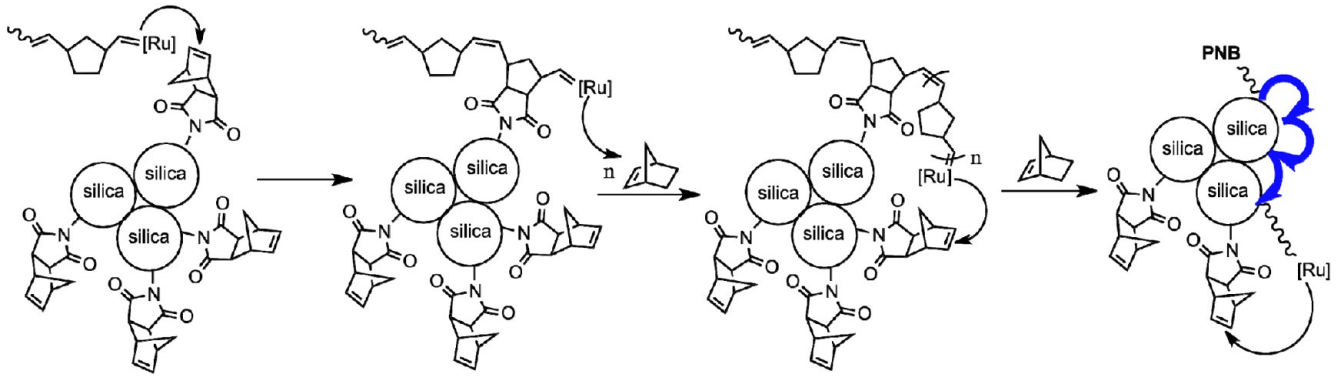

[a][Ru]: Grubbs' catalyst coordinated at the head of a propagating polymer chain; in blue (part B): polymeric stitches by engaging and incorporating surface-norbornene moieties within propagating polynorbornene chains.

Table 4. Materials Properties of the Si-NAD Derived Aerogels and the Controls (Native n-TMOS and n-TMOS-co-APTES)

sample	polymer,[a] % w/w	skeletal density, ρ_s[b] (g cm^{-3})	closed skeletal porosity,[c] $\%V_{CP}$ (v/v)	monolith linear shrinkage[d,e] (%)	bulk density, ρ_b[d] (g cm^{-3})	open bulk porosity, Π (% void space)	BET surface area, σ (m^2 g^{-1})	average pore diameter[f] (nm)	BJH pore diameter[g] (nm)	particle radius, r_p[h] (nm)
n-SiNAD	*i*	1.811 ± 0.007		6 ± 0.7	0.197 ± 0.005	89.1	590	25.4 [30.7]	41.5 [24.0]	2.8
X-SiNAD(10)	16	1.60_9 ± 0.01_3	1.6	13 ± 1	0.273 ± 0.009	83.0	368	25.3 [33.1]	38.6 [13.0]	5.1
X-SiNAD(20)	26	1.505 ± 0.003	3.8	20 ± 0.5	0.38_2 ± 0.01_1	74.6	243	18.9 [32.2]	22.2 [6.9]	8.2
X-SiNAD(30)	38	1.391 ± 0.004	5.6	27 ± 1	0.63_2 ± 0.02_0	54.6	124	14.2 [27.8]	16.1 [3.2]	17.4
n-TMOS	*i*	1.970 ± 0.007		13.0	0.200	89.8	724	19.6 [24.8]	20.7 [2.8]	2.1
n-TMOS-co-APTES	*i*	1.835 ± 0.003		8 ± 0.5	0.196 ± 0.002	89.3	491	12.4 [37.1]	13.4 [3.6]	3.3

[a]By TGA (Figure 3); for calculations, see Appendix II in Supporting Information. [b]Single sample, average of 50 measurements. [c]Via eq 6. [d]Average of three samples. [e]Linear shrinkage =100 × (sample diameter − mold diameter)/(mold diameter). [f]By the $4 \times V_{Total}/\sigma$ method. For the first number, V_{Total} was calculated by the single-point adsorption method; for the number in brackets, V_{Total} was calculated via $V_{Total} = (1/\rho_b) - (1/\rho_s)$. [g]From the desorption branch of the isotherm. The first number is the peak maxima; the number in brackets is the full width at the half maximum. [h]Calculated via $r = 3/\rho_s\sigma$. [i]Not applicable.

(Table 4). Qualitatively, macroporosity created a divergence of the average pore sizes calculated via the $4 \times V_{Total}/\sigma$ method, whereas the total volume of N_2 adsorbed, V_{Total}, either is taken from the highest point of the adsorption isotherm at $(P/P_0 \sim 1)$, or is calculated via $V_{Total} = (1/\rho_b) - (1/\rho_s)$. With regards to both the n- and all X-samples, the average pore sizes calculated by the two methods are equally close to one another (Table 4). This finding suggests that we are dealing primarily with mesoporous materials (i.e., pore sizes in the 2−50 nm range). Indeed, all N_2-sorption isotherms (Figure 8) showed desorption hysteresis loops. Those isotherms can be classified as Type IV characterizing mesoporous materials. Upon closer examination, though, the isotherms of **n-SiNAD** do not reach saturation, in agreement with the macroporosity noted in FESEM. On the other hand, the isotherms of all X-samples did reach saturation, suggesting that macroporosity had been eliminated. Furthermore, as the amount of polymer increased, the desorption branch turns from H1-type (unobstructed adsorption−desorption, **X-SiNAD(10)** and **X-Si-NAD(20)** samples) into H2-type (ink-bottle-like pores, **X-SiNAD(30)** samples). All X-samples, however, remained mesoporous, as the *t*-plot analysis shows no indication for open microporosity (pore diameters < 2 nm) in any sample. By the same token, along the process of ink-bottle pore formation, it is reasonable

dx.doi.org/10.1021/cm3017648 | *Chem. Mater.* 2012, 24, 3434−3448

that some bottle-necks might get closed. That could explain the small amount of closed porosity identified via skeletal density considerations above.

Pore size distributions were evaluated by the BJH method applied on the desorption branch of the isotherms. (Plots are given as insets in Figure 8.) The maxima of the BJH plots are in good agreement with those from the $4 \times V_{Total}/\sigma$ method applied to the maximum volume of N_2 adsorbed (see Table 4). The native **n-SiNAD** samples also show a shoulder at the smaller pore size of the BJH curve (~30 nm, indicated with an arrow in Figure 8), suggesting two kinds of mesopores. That shoulder is progressively eliminated in the X-samples, suggesting a closing of the smaller pores. The elimination of smaller pores should have shifted average pore sizes to larger values. The opposite, however, was observed, presumably as the result of a contraction (shrinking) of the entire structure.

As previously discussed, the simple accumulation of polymer on the skeletal framework of **X-SiNAD(xx)** samples would increase the stiffness (resistance to bending). As opposed to simple polymer accumulation, bridging skeletal nanoparticles covalently would increase the ultimate strength of the whole structure.[9] Indeed, under compression, all NB-cross-linked **X-NB-Si-NAD** aerogels were not only much stiffer (108–386 MPa vs 5.3 MPa) but also much stronger (19–59 MPa vs 4.5 MPa) and tougher (14.5–23.2 J g^{-1} vs 5.7 J g^{-1}) than **n-SiNAD**. The elastic (Young's) modulus, E, increases exponentially with the bulk density, ρ_b, according to a power law of the form $E \sim \rho_b^{1.5}$ (see Figure 9). (It is noted though that the power-law exponent is lower than what has been reported for silica (3.7),[43] *thus underlining the efficiency of low polymer loadings for increasing strength.*) Even more intriguing is the behavior of both the ultimate compressive strength (UCS) and the energy absorption as functions of bulk density (both shown by log–log plots in Figure 9); after an initial jump from **n-SiNAD** to **X-SiNAD(10)**, these properties remained nearly constant for **X-SiNAD(20)**, increasing drastically thereafter for **X-SiNAD(30)**. The slopes of the log–log plots between **X-SiNAD(20)** and **X-SiNAD(30)** are 1.92 and 1.03 for the UCS and energy absorption, respectively, in line with silica (for which the values are 2.6 and 1.6, respectively, albeit in a 3-point bending configuration).[43] The discontinuity in the log–log plots for both UCS and energy absorption suggests that not all polymer is equivalent: polymer accumulating at the early stages of cross-linking has a different effect from that accumulating later. Hence, both indentifying possible chemical differences and locating the two kinds of polynorbornene on the silica nanostructure are important.

As inferred by the microscopic similarity of **n-SiNAD** to all three **X-SiNAD(xx)** (Figure 8), the polymer is always closely associated with silica. That fact, in combination with covalent bonding between the two, should restrict segmental motion of polymeric strands and, therefore, raise the glass transition temperature, T_g, relative to the bulk polymer as the thickness of the polymeric cross-linker decreases.[44] Indeed, as shown in Figure 10, **X-SiNAD(10)** had the highest T_g (73.8 °C). That value decreased sharply to 63.9 °C for **X-SiNAD(20)**, eventually reaching 60.6 °C for **X-SiNAD(30)**. This temperature is still higher than the T_g of free polymer formed and collected from the cross-linking bath (50.4 °C). Clearly, the polymer in all three X-samples never reached a thickness high enough to behave as bulk NB. In a careful comparison of grafted brushes versus cast PMMA films, Yamamoto et al. demonstrated that a 10 °C higher T_g [an analogous situation to

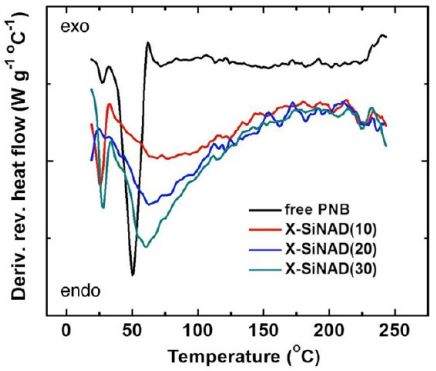

Figure 10. Modulated differential scanning calorimetry (MDSC) data under N_2 at 10 °C min^{-1}. (For additional parameters, see Experimental Section.)

X-SiNAD(30)] corresponds to layers of brushes approximately 10 nm thick.[44c] In terms of the **n-SiNAD** nanostructure, this thickness is within secondary particles. Finally, the full width at half maximum of the heat exchange profiles of the three X-samples was much broader (42–67 °C) than that of the free polymer (12 °C), reflecting the variable lengths between points of attachment of the polymer to the silica backbone.

The cross-linking polymer was freed from the silica framework of all three X-samples by treatment with HF. The free polymer was extracted with $CHCl_3$, and its size was investigated with gel permeation chromatography (GPC) in THF using polystyrene standards. Results were compared to free polymer formed outside the gels in the surrounding cross-linking bath. (Owing to similar hydrodynamic radii in THF of both polynorbornene and polystyrene at equal molecular weights, the latter was a good model for the former.[45]) Typical GPC data are given in Figure 11. All results are summarized in Table S.1 in Supporting Information. By inspection, peaks corresponding to individual polymers/oligomers were placed in both a lower retention time group (R_f ~ 6.5 min, higher molecular weight polymer) and a higher R_f group (~9.7 min, smaller oligomers). Those two groups were fitted to Gaussian profiles (indicated with dashed lines in Figure 11). Average molecular weights were calculated by standard procedures.[29] The long component varied from 379 to 505 monomer units; its weight percent contribution increases from 32% in **X-SiNAD(10)** to 41% in **X-SiNAD(20)** to 50% in **X-SiNAD(30)**, while the polydispersity remained relatively low, in the 1.88–2.28 range. The short component, however, had only 8–11 monomer units and a polydispersity of 1.74–2.53. The makeup of the polymer formed in the cross-linking bath was somewhat different from that formed on the skeletal framework; that polymer included a third major fraction (50% w/w), with intermediate retention time (R_f ~ 8.4 min) corresponding to ~100 monomer units with very high polydispersity (7–10). In contrast to the X-samples, the distribution of the three fractions in the polymer from the cross-linking bath did not change with the concentration, advocating for the role of surface-NB in modulating the polymer length in the gels through the stitching mechanism of Scheme 3. The radii of gyration, R_g, of the polymer fractions freed from the network were calculated both for good (swelling) solvents via eq 7[46] and for theta solvents via eq 8,[47] where the number of monomer units, N, is taken from Table S.1 in Supporting Information and the length of the monomer repeat unit, α, was found by simulation equal to 4.85 Å.

dx.doi.org/10.1021/cm3017648 | *Chem. Mater.* 2012, 24, 3434–3448

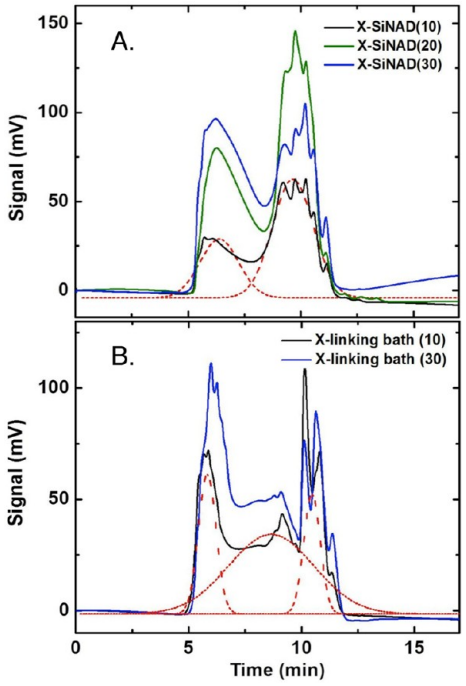

Figure 11. Gel permeation chromatographic (GPC) analysis of polymer extracted from cross-linked samples (A) and of polymer formed and isolated from two cross-linking baths, as indicated (B). For details, refer to the Experimental Section. Eluted peaks are segregated into a low and a high retention time cluster, which are fitted to Gaussian profiles, as indicated by the dashed curves. Complete data analysis is available in Table S.1 of Supporting Information.

$$R_{g\_swelling} = \frac{a}{6^{1/2}} N^{3/5} \quad (7)$$

$$R_{g\_theta} = \frac{a}{6^{1/2}} N^{1/2} \quad (8)$$

Three models are thus consistent with the data (Scheme 4). Model I is based on the polymerization chemistry outlined in Scheme 3, which is expected to form a polymer shell around NB-modified silica cores. Model II expands on Model I by considering that the polymer may form lumps distributed within the empty space (see Table 2) of secondary particles. In Model III, an alternative to Model II, most of the space within the secondary particles is filled evenly by polymer; some void space, in the form of closed pores, is consistent with the polymer content/skeletal density considerations above.

If the polymer coils up (Model II), the radius of gyration calculated for theta solvents, R_{g_theta}, may be considered an upper bound for the radius of gyration of possible dry spherical lumps. Those radii of gyration are included in Table S.1, Supporting Information. They were used to calculate the radii of the hypothetical lump, which, for the short polymer component, were 0.73−0.86 nm, and for the long component in the range of 5.0−5.8 nm. TEM as a tool to look directly inside secondary particles in hopes to see those polymer spheres was inconclusive, probably because of the small Z-attenuation difference between silica and polymer:[48] according to Figure S.4 in Supporting Information, upon polymer uptake images get blurry, and the sharp definition of silica particles is lost, but yet they appear surrounded by an unstructured sort of matrix. Thus, to glimpse inside the secondary particles, we resorted back to SAXS/SANS (Figure 6 and Table 2) in combination with some selected general material characterization data from Table 4.

Scheme 4. Models for Secondary Particles in X-SiNAD(xx) Aerogels[a]

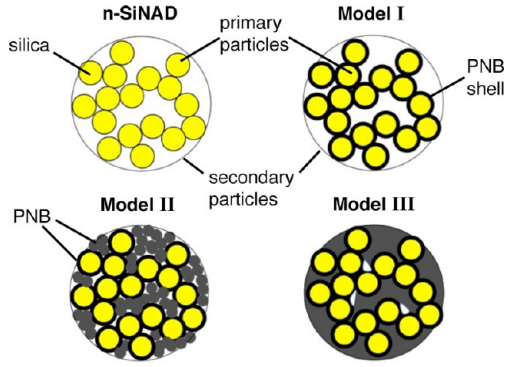

[a]Model I: secondary particles consist of silica-core/polymer-shell primary particles; Model II: in addition to Model I, secondary particles include lumps of polynorbornene; Model III: an alternative to Model II, whereas polymer is evenly distributed around the core/PNB−shell primary particles of Model I. (The illustration emphasizes also the fact that secondary particles may include closed pores. See text related to eq 6.)

By SANS/SAXS, all three cross-linked samples continued to demonstrate the same hierarchical primary/fractal-secondary particle structure of **n-SiNAD**. Of major importance is the fact that primary particles were discernible at all. Thus, those particles were embedded in a medium of different density ($\Delta\rho \neq 0$, refer to eq 4). The radius of the primary particles increased monotonically with the degree of cross-linking from **X-SiNAD(10)** to **X-SiNAD(30)**. The radius of the secondary particles first decreased from 28.7 ± 0.3 nm in **n-SiNAD** to ∼21 nm in **X-SiNAD(10)** and **X-SiNAD(20)** and then increased to 29.1 ± 0.4 nm in **X-SiNAD(30)**. The uncertainties (error) in the radii of gyration of the primary particles were less than 4% in SAXS, 7% in SANS, and, in most cases, less than 2%. Hence, we are dealing with only one kind of primary particles. Should the polymer have coiled into 5.0−5.8 nm lumps, those lumps would have interfered with the scattering profile of the silica primary particles, yielding bimodal particle size distributions. The latter were not detected. Therefore, discrete polymeric lumps (Model II, Scheme 4) were not formed at any level. On the contrary, primary particles in the cross-linked samples still show fuzzy (density-gradient) interfaces (high-Q slopes > 4.0), and the thicknesses of the fuzzy zones are very similar to those of the native **n-SiNAD** samples (6.0−6.8 Å versus 5.0 Å, respectively).

To this point in the study, the SAXS/SANS data have been consistent with polymer building into a tight, dense conformal shell (coating) around the silica core primary particles comprising the native **n-SiNAD** network. That coating covalently bridges, as designed, primary particles, pulling them together so that secondary particles contract. As outlined in Appendix III of the Supporting Information, the radius of the core−shell primary particles can be calculated from the radius of the native primary particles (7.71 nm by SAXS), the skeletal density of the silica core (1.811 g cm^{-3}), and the density of the polynorbornene isolated from the cross-linking bath (ρ_{PNB} = 1.129 g cm^{-3}). It was thus found for the ratios (experimental radius by SAXS/calculated radius, nm/nm) 7.7/8.7 for **X-SiNAD(10)**; 8.2/9.4 for **X-SiNAD(20)**; and, 9.4/10.6 for **X-SiNAD(30)**. The values in the pairs are close, providing support for the formation of

dx.doi.org/10.1021/cm3017648 | *Chem. Mater.* 2012, 24, 3434−3448

polynorbornene shells around the primary silica core particles of the native **n-SiNAD** framework.

The medium surrounding the primary core−shell particles within the secondary particles may be either air or looser polymer of different density from that forming the core−shell structure around primary particles (Model III). The GPC analysis above corroborates with this model, suggesting a succession of events: NB moieties on primary particles are engaged early, leading to a conformal coating of shorter, closely held (denser) polymer. Longer polymer fills the empty space within secondary particles. The immediate question then is whether or not secondary particles are completely filled with polymer. As discussed in Section 3.a, owing to their fractal structure, secondary particles of **n-SiNAD** consist of 78% empty space. Similarly, "empty" space within secondary particles of X-samples can also be calculated from the experimental radii of gyration of the core−shell primary particles and is cited in Table 2. Owing to the uncertainties involved, for that calculation we assumed that the fractal dimension of all secondary particles remained equal to that of **n-SiNAD** (D_f = 2.07). At first approximation, that is, by ignoring closed pores, an assessment of whether that "empty" space is filled with polynorbornene can be obtained by comparing the experimental skeletal densities of the X-samples (Table 4) with those calculated as the weighted average of silica and polymer and assuming that all the space surrounding primary particles is occupied by polymer. Additional assumptions are that (a) secondary particles consist of primary silica particles of the same dimensions found in **n-SiNAD** (7.71 nm by SAXS) and (b) space is filled by one kind of polymer, that obtained from the cross-linking bath. We thus find for the ratios (experimental/calculated skeletal densities, g cm^{-3}/g cm^{-3}) 1.609/1.327 for **X-SiNAD(10)**; 1.505/1.327 for **X-SiNAD(20)**; and 1.391/1.279 for **X-SiNAD(30)**. The two skeletal densities converge for **X-SiNAD(30)**. Looking at the issue from a different perspective, the smallest particle radii, *r*, calculated from both skeletal densities and BET surface areas (values included in Table 4) agree reasonably well with the radii of the core−shell primary particles estimated from SAXS for **X-SiNAD(10)** and **X-SiNAD(20)**, but they jump to higher values for **X-SiNAD(30)**, consistent with mostly polymer-filled secondary particles. Overall, data converge toward Model III for higher PNB loadings.

4. CONCLUSION

The experimental implementation in 2002 of Mackenzie's 1992 conjecture calling for polymer/sol−gel composites consisting of polymeric tethers bridging interconnected silica particles[49] produced polymer-cross-linked aerogels, a class of extremely strong, yet lightweight materials.[3b] However, given the complex hierarchical structure of silica (agglomerates of porous, fractal secondary nanoparticles), the exact location of the polymer and, therefore, application-specific questions such as how much is enough had not been addressed yet. Here, by designing a system where cross-linking takes place by a well-defined process (grafting-to ROMP), loose polymer can be removed easily. Then, by using a wide array of characterization methods, it is concluded that accumulation of the cross-linking polymer follows the hierarchical structure of silica (Model III, Scheme 4). The polymer stays close, forming a conformal coating around primary particles. Subsequently, it fills secondary particles without formation of globules or lumps. Along that process, only a very small amount of closed porosity is created (<5% v/v of the skeletal network). Most importantly, however, a small amount of polymer (e.g., 16% w/w) that coats only primary particles with minimal compromise in the overall porosity (from 89% to 83% v/v) and the porosity-related properties (e.g., BET surface areas, from 590 to 368 m^2 g^{-1}) is enough to increase stiffness by a factor of 20× and ultimate compressive strength by a factor of 4×. At that point, silica aerogels are quite robust materials, making them easy to handle. Additional polymer continues to accumulate, mostly on and around primary particles, so that properties such as porosity and BET surface area begin decreasing noticeably without any gain in either ultimate compressive strength or specific energy absorption. The point where mechanical properties start improving drastically again is when secondary particles are almost completely filled with polymer. The subject matter of this paper, that is, the detailed correlation of structure-mechanical strength at the early stages of cross-linking, raises obvious questions about the opposite end of the strength-density continuum, namely for materials classified as polymer−matrix composites.[50]

■ ASSOCIATED CONTENT

Supporting Information

Rheology during base-catalyzed gelation of TMOS (Figure S.1); IR spectra of representative aerogel samples (Figure S.2); overlaid SAXS and SANS data for **n-SiNAD** (Figure S.3); TEM data for **X-SiNAD(xx)** (Figure S.4); GPC analysis data (Table S.1); calculation of empty space in secondary particles (Appendix I); calculation of polymer content in X-samples from TGA data (Appendix II); and calculation of the thickness of a polymer shell around a silica core from experimental skeletal density data (Appendix III). This information is available free of charge via the Internet at http://pubs.acs.org.

■ AUTHOR INFORMATION

Corresponding Author

*E-mail: leventis@mst.edu (N.L.), cslevent@mst.edu (C.S.-L.), jtmang@lanl.gov (J.T.M.), hongbing.lu@utdallas.edu (H.L.).

Notes

The authors declare no competing financial interest.

■ ACKNOWLEDGMENTS

This project was supported by the Army Research Office under Award No. W911NF-10-1-0476. Initial funding was provided by the National Science Foundation under Agreement No. CHE-0809562. H. Lu acknowledges the support of NSF under CMMI-1031829 & 1132174. We would also like to thank both Ms. Clarissa Wisner for her help with TEM and Dr. Wei Wycoff of the University of Missouri Columbia for her help with the solids NMR. This work benefited from the use of the SANS instrument, LQD, at the Manuel Lujan, Jr., Neutron Scattering Center of the Los Alamos National Laboratory, supported by the DOE office of Basic Energy Sciences, and utilized facilities supported in part by the National Science Foundation under Agreement No. DMR-0454672.

■ REFERENCES

(1) (a) Pierre, A. C.; Pajonk, G. M. *Chem. Rev.* **2002**, *102*, 4243−4265. (b) Morris, C. A.; Anderson, M. L.; Stroud, R. M.; Merzbacher, C. I.; Rolison, D. R. *Science* **1999**, *284*, 622−624.

(2) (a) Kistler, S. S. *Nature* **1931**, *127*, 741. (b) Kistler, S. S. *J. Phys. Chem.* **1932**, *36*, 52−64. (c) Gurav, J. L.; Rao, A. V.; Rao, A. P.; Nadargi, D. Y.; Bhagat, S. D. *J. Alloys Compd.* **2009**, *476*, 397−402. (d) Rao, A. V.; Bangi, U. K. H.; Kavale, M. S.; Imai, H.; Hirashima, H. *Microporous Mesoporous Mater.* **2010**, *134*, 93−99.

(3) (a) Leventis, N.; Sotiriou-Leventis, C.; Zhang, G.; Rawashdeh, A-M. M. *Nano Lett.* **2002**, *2*, 957−960. (b) Leventis, N. *Acc. Chem. Res.* **2007**, *40*, 874−884. (c) Leventis, N.; Lu, H. Polymer-Crosslinked Aerogels. In *Aerogels Handbook*; Aegerter, M. A., Leventis, N., Koebel, M. M., Eds.; Springer: New York, 2011; pp 251−285.
(4) (a) Leventis, N.; Vassilaras, P.; Fabrizio, E. F.; Dass, A. *J. Mater. Chem.* **2007**, *17*, 1502−1508. (b) Leventis, N.; Sotiriou-Leventis, C.; Mulik, S.; Dass, A.; Schnobrich, J.; Hobbs, A.; Fabrizio, E. F.; Luo, H.; Churu, G.; Zhang, Y.; Lu, H. *J. Mater. Chem.* **2008**, *18*, 2475−2482. (c) Leventis, N.; Chandrasekaran, N.; Sotiriou-Leventis, C.; Mumtaz, A. *J. Mater. Chem.* **2009**, *19*, 63−65. (d) Leventis, N. Interpenetrating Organic/Inorganic Networks of Resorsinol-Formaldehyde/Metal Oxide Aerogels. In *Aerogels Handbook*; Aegerter, M. A., Leventis, N., Koebel, M. M., Eds.; Springer: New York, 2011; pp 287−313.
(5) Lu, H.; Luo, H.; Leventis, N. Mechanical Characterization of Aerogels. In *Aerogels Handbook*; Aegerter, M. A., Leventis, N., Koebel, M. M., Eds.; Springer: New York, 2011; pp 499−535.
(6) Leventis, N.; Palczer, A.; McCorkle, L.; Zhang, G.; Sotiriou-Leventis, C. *J. Sol-Gel Sci. Tech.* **2005**, *35*, 99−105.
(7) Leventis, N.; Sadekar, A.; Chandrasekaran, N.; Sotiriou-Leventis, C. *Chem. Mater.* **2010**, *22*, 2790−2803.
(8) Hüsing, N.; Schubert, U. *Angew. Chem., Int. Ed.* **1998**, *37*, 22−45.
(9) Mulik, S.; Sotiriou-Leventis, C.; Churu, G.; Lu, H.; Leventis, N. *Chem. Mater.* **2008**, *20*, 5035−5046.
(10) Boday, D. J.; Keng, P. Y.; Muriithi, B.; Pyun, J.; Loy, D. A. *J. Mater. Chem.* **2010**, *20*, 6863−6865.
(11) Boday, D. J.; DeFriend, K. A.; Wilson, K. V.; Coder, D.; Loy, D. A. *Chem. Mater.* **2008**, *20*, 2845−2847.
(12) Zhang, G.; Dass, A.; Rawashdeh, A-M. M.; Thomas, J.; Counsil, J. A.; Sotiriou-Leventis, C.; Fabrizio, E. F.; Ilhan, F.; Vassilaras, P.; Scheiman, D. A.; McCorkle, L.; Palczer, A.; Johnson, J. C.; Meador, M. A. B.; Leventis, N. *J. Non-Cryst. Solids* **2004**, *350*, 152−164.
(13) (a) Katti, A.; Shimpi, N.; Roy, S.; Lu, H.; Fabrizio, E. F.; Dass, A.; Capadona, L. A.; Leventis, N. *Chem. Mater.* **2006**, *18*, 285−296. (b) Meador, M. A. B.; Capadona, L. A.; McCorkle, L.; Papadopoulos, D. S.; Leventis, N. *Chem. Mater.* **2007**, *19*, 2247−2260.
(14) Meador, M. A. B.; Fabrizio, E. F.; Ilhan, F.; Dass, A.; Zhang, G.; Vassilaras, P.; Johnston, J. C.; Leventis, N. *Chem. Mater.* **2005**, *17*, 1085−1098.
(15) See for example: Ilhan, F.; Fabrizio, E. F.; McCorkle, L.; Scheiman, D.; Dass, A.; Palczer, A.; Meador, M. A. B.; Johnston, J. C.; Leventis, N. *J. Mater. Chem.* **2006**, *16*, 3046−3054.
(16) (a) Guo, H.; Nguyen, B. N.; McCorkle, L. S.; Shonkwiler, B.; Meador, M. A. B. *J. Mater. Chem.* **2009**, *19*, 9054−9062. (b) Nguyen, B. N.; Meador, M. A. B.; Tousley, M. E.; Shonkwiler, B.; McCorkle, L.; Sceiman, D. A.; Palczer, A. *ACS Appl. Mater. Interfaces* **2009**, *1*, 621−630.
(17) (a) Leventis, N.; Chandrasekaran, N.; Sadekar, A. G.; Sotiriou-Leventis, C.; Lu, H. *J. Am. Chem. Soc.* **2009**, *131*, 4576−4577. (b) Leventis, N.; Chandrasekaran, N.; Sadekar, A. G.; Mulik, S.; Sotiriou-Leventis, C. *J. Mater. Chem.* **2010**, *20*, 7456−7471.
(18) Grubbs, R. H. *Angew. Chem., Int. Ed.* **2006**, *45*, 3760−3765.
(19) (a) Lee, J. K.; Gould, G. L. *J. Sol-Gel Sci. Technol.* **2007**, *44*, 29−40. (b) Dawedeit, C.; Kim, S. H.; Braun, T.; Worsley, M. A.; Letts, S. A.; Wu, K. J.; Walton, C. C.; Chernov, A. A.; Satcher, J. H.; Hamza, A. V.; Biener, J. *Soft Matter* **2012**, *8*, 3518−3521.
(20) (a) Juang, A.; Scherman, O. A.; Grubbs, R. H.; Lewis, N. S. *Langmuir* **2001**, *17*, 1321−1323. (b) Harada, Y.; Girolami, G. S.; Nuzzo, R. G. *Langmuir* **2003**, *19*, 5104−5114. (c) Kim, N. Y.; Jeon, N. L.; Choi, I. S.; Takami, S.; Harada, Y.; Finnie, K. R.; Girolami, G. S.; Nuzzo, R. G.; Whitesides, G. M.; Laibinis, P. E. *Macromolecules* **2000**, *33*, 2793−2795.
(21) (a) Kong, B.; Lee, J. K.; Choi, I. S. *Langmuir* **2007**, *23*, 6761−6765. (b) Weck, M.; Jackiw, J. J.; Rossi, R. R.; Weiss, P. S.; Grubbs, R. H. *J. Am. Chem. Soc.* **1999**, *121*, 4088−4089.
(22) Watson, K. J.; Zhu, J.; Nguyen, S. T.; Mirkin, C. A. *J. Am. Chem. Soc.* **1999**, *121*, 462−463.
(23) Jeong, W.; Kessler, M. R. *Chem. Mater.* **2008**, *20*, 7060−7068.
(24) Buchmeiser, M.; Sinner, F.; Mupa, M.; Wurst, K. *Macromolecules* **2000**, *33*, 32−39.
(25) Pavia, D. L.; Lampman, G. M.; Kriz, G. S.; Engel, R. G. A Small Scale Approach to Organic Laboratory Techniques, 3rd ed.; Brooks Cole: Independence, KY, 2010; pp 405−409.
(26) Leventis, N.; Elder, I. A.; Rolison, D. R.; Anderson, A. L.; Merzbacher, C. I. *Chem. Mater.* **1999**, *11*, 2837−2845.
(27) Seeger, P. A.; Hjlem, R. P., Jr. *J. Appl. Crystallogr.* **1991**, *24*, 467−478.
(28) Ilavsky, J.; Jemian, P. R. *J. Appl. Crystallogr.* **2009**, *42*, 347−353.
(29) (a) Harmon, D. J. *J. Polym. Sci.* **1965**, *C8*, 243−251. (b) May, J. A., Jr.; Smith, W. B. *J. Phys. Chem.* **1968**, *72*, 216−221.
(30) Winter, H. H. *Polym. Eng. Sci.* **1987**, *27*, 1698−1702.
(31) Kim, S.-Y.; Choi, D.-G.; Yang, S.-M. *Korean J. Chem. Eng.* **2002**, *19*, 190−196.
(32) Raghavan, S. R.; Chen, L. A.; McDowell, C.; Khan, S. A.; Hwang, R.; White, S. *Polymer* **1996**, *37*, 5869−5875.
(33) Muthukumar, M. *Macromolecules* **1989**, *22*, 4656−4658.
(34) Kolb, M.; Botet, R.; Julien, J. *Phys. Rev. Lett.* **1983**, *51*, 1123−1126.
(35) See for example: (a) Mazúr, M.; Mlynárik, V.; Valko, M.; Pelikán, P. *Appl. Magn. Reson.* **1999**, *16*, 547−557. (b) Corminbœuf, C.; Heine, T.; Weber, J. *Chem. Phys. Lett.* **2002**, *357*, 1−7. (c) El hadad, A. A.; Carbonell, D.; Barranco, V.; Jiménez-Morales, A.; Casal, B.; Galván, J. C. *Colloid Polym. Sci.* **2011**, *289*, 1875−1883.
(36) Hench, L. L.; West, J. K. *Chem. Rev.* **1990**, *90*, 33−72.
(37) Hüsing, N.; Schubert, U.; Mezei, R.; Fratzl, P.; Riegel, B.; Kiefer, W.; Kohler, D.; Mader, W. *Chem. Mater.* **1999**, *11*, 451−457.
(38) Koberstein, J. T.; Morra, B.; Stein, R. S. *J. Appl. Crystallogr.* **1980**, *13*, 34−45.
(39) Guinier, A.; Fournet, G. *Small-Angle Scattering of X-rays*; John Wiley and Sons: New York, NY, 1955.
(40) (a) Beaucage, G. *J. Appl. Crystallogr.* **1995**, *28*, 717−728. (b) Beaucage, G. *J. Appl. Crystallogr.* **1996**, *29*, 134−146. (c) Mang, J. T.; Son, S. F.; Hjelm, R. P.; Peterson, P. D.; Jorgensen, B. S. *J. Mater. Res.* **2007**, *22*, 1907−1920.
(41) Lee, D. G.; Bonner, J. S.; Garton, L. S.; Ernest, A. N. S.; Autenrieth, R. L. *Water Res.* **2000**, *34*, 1987−2000.
(42) Kucheyev, S. O.; Stadermann, M.; Shin, S. J.; Satcher, J. H., Jr.; Gammon, S. A.; Letts, S. A.; van Buuren, T.; Hamza, A. V. *Adv. Mater.* **2012**, *24*, 776−780.
(43) Woignier, T.; Phalippou, J. *Rev. Phys. Appl.* **1989**, *24*, 179−184.
(44) See for example: (a) Vyazovkin, S.; Dranca, I.; Fan, X.; Advincula, R. *J. Phys. Chem. B* **2004**, *108*, 11672−11679. (b) Blum, F. D.; Young, E. N.; Smith, G.; Sitton, O. C. *Langmuir* **2006**, *22*, 4741−4744. (c) Yamamoto, S.; Tsujii, Y.; Fikuda, T. *Macromolecules* **2002**, *35*, 6077−6079.
(45) Jordi, M. A.; Seery, T. A. P. *J. Am. Chem. Soc.* **2005**, *127*, 4416−4422.
(46) Ken, T.; Mays, J. W. *Eur. Polym. J.* **2004**, *40*, 1623−1627.
(47) Peterson, K. A.; Zimmt, M. B.; Linse, S.; Dominique, R. P.; Fayer, M. D. *Macromolecules* **1987**, *20*, 168−175.
(48) See for example: (a) Ribbe, A.; Prucker, O.; Rühe, J. *Polymer* **1996**, *37*, 1087−1093. (b) Midgley, P. A.; Ward, E. P. W.; Hungría, A. B.; Thomas, J. M. *Chem. Soc. Rev.* **2007**, *36*, 1477−1494. (c) Chen, Z.; Gang, T.; Zhang, K.; Zhang, J.; Chen, X.; Sun, Z.; Yang, B. *Colloids Surf., A* **2006**, *272*, 151−156. (d) Hao, L.; Zhu, C.; Chen, C.; Kang, P.; Hu, Y.; Fan, W.; Chen, Z. *Synth. Met.* **2003**, *139*, 391−396.
(49) Hu, Y.; Mackenzie, J. D. *J. Mater. Sci.* **1992**, *27*, 4415−4420.
(50) Leventis, N.; Sotiriou-Leventis, C.; Mulik, S.; Patil, V.; Mohite, D.; Zhang, Y.; Lu, H. *Polym. Prepr.* **2008**, *49*, 504−506.